Pulse Compression and Sea Level Tracking in Satellite Altimetry

DUDLEY B. CHELTON,* EDWARD J. WALSH** AND JOHN L. MACARTHUR†

(Manuscript received 2 August 1988, in final form 6 October 1988)

ABSTRACT

With the presently operational altimeter on the U.S. Navy satellite GEOSAT, and three new altimeters soon to be launched by the European, French and U.S. space agencies, satellite altimetry promises to become a standard technique for studying oceanographic variability. Little has been written about the instrumental technique used to determine sea surface height from altimetric measurements. In this paper, we summarize the pulse-compression technique by which a radar altimeter transmits a relatively long pulse and processes the returned signal in a way that is equivalent to transmitting a very short pulse and measuring the time history of the returned power in a sequence of range gates. The effective short pulse enhances the range resolution that would be obtained from the actual long pulse. The method used onboard the satellite to track the point on the returned signal corresponding to the range to mean sea level (spatially averaged over the altimeter footprint) is also summarized. Pulse compression and sea level tracking are important to the overall error budget for altimetric estimates of sea level. The dominant sources of sea level tracking errors are discussed, with particular emphasis on the high degree of accuracy required for the TOPEX altimeter scheduled for launch in mid 1992. Also included here as an appendix is a derivation of the spherical earth correction to altimeter footprint area. It is shown that the flat earth approximation used heretofore in ground-based processing of altimeter data results in a bias of −0.51 dB in estimates of normalized radar cross section from an altitude of 800 km; if not corrected, this bias would increase to −0.83 dB for the TOPEX altitude of 1335 km.

1. Introduction

Over the next four years, three new satellite altimeters will be launched into space for ocean circulation research applications. The European Space Agency has an expected launch in mid 1991 for the ERS-1 satellite, which includes an altimeter in its suite of four instruments. The U.S. National Aeronautics and Space Administration (NASA) and the French Centre National d'Etudes Spatiales (CNES) will jointly launch the NASA TOPEX and CNES POSEIDON altimeters on a dedicated altimetric mission scheduled for a mid 1992 launch. These three new altimeters follow a long heritage of satellite altimeters, beginning with SKYLAB in 1973 (McGoogan et al. 1974), followed by GEOS-3 from April 1975 to December 1978 (Stanley 1979), and SEASAT from July to October 1978 (Tapley et al. 1982). Presently, the GEOSAT altimeter (MacArthur et al. 1987) has been providing useful altimetric measurements since March 1985.

The basic principle of satellite altimetry is conceptually straightforward. A radar altimeter precisely measures the range from the radar antenna to the ocean surface. From an oceanographic perspective, the primary application of satellite altimetry is to measure the sea surface elevation (height) resulting from geostrophic ocean currents, which requires an overall accuracy of a few 10 cm. The altimeter transmits a short pulse of microwave radiation with known power toward the sea surface at satellite nadir (the point directly beneath the satellite). This pulse interacts with the sea surface and part of the incident radiation reflects back to the satellite. The range from the satellite to the sea surface is determined from the two-way travel time of the pulse. In addition, estimates of near-surface wind speed and wave height can be obtained from altimeter data. This paper summarizes the range measurement technique, with some discussion of altimeter estimates of wave height determined from the shape of the returned signal. For a discussion of altimeter estimates of wind speed from the power of the returned signal (the radar cross section), see Chelton and McCabe (1985) and Chelton and Wentz (1986).

Over the time span since the SKYLAB altimeter, technological developments have transformed satellite radar altimetry from a technique by which major geoid features with order 10 m amplitude could be resolved

---

* College of Oceanography, Oregon State University, Corvallis, Oregon.

** NASA Goddard Space Flight Center, Greenbelt, Maryland. (Presently on assignment at: NOAA Wave Propagation Laboratory, Boulder, Colorado.)

† The Johns Hopkins University, Applied Physics Laboratory, Laurel, Maryland.

Corresponding author address: Dudley B. Chelton, College of Oceanography, Oregon State University, Corvallis, OR 97331.

to one where resolution of dynamic ocean signals as small as a few cm is possible in 1-s averages of the height measurements (TOPEX Science Working Group 1981). These improvements in the accuracy of satellite altimeter height measurements are among the most significant technological advancements that have made possible the global perspective of the World Ocean Circulation Experiment planned for the 1990s (Briscoe 1986; Nowlin 1987). In particular, the NASA TOPEX altimeter (MacArthur and Brown 1984) has been carefully designed with a goal of achieving an accuracy of better than 2-cm rms for each individual component of the height measurement (excluding orbit error, which is expected to have an accuracy of 13 cm). Such high degree of accuracy from an altimeter orbiting the earth at an altitude of about 1335 km pushes the limits of present technology.

The technique by which the sea surface topography associated with ocean currents is measured by an altimeter is very complex, involving more than a dozen corrections for effects such as instrumental biases, atmospheric refraction, and external geophysical effects on the sea surface topography that are unrelated to ocean circulation (gravity, tides, and atmospheric pressure loading of the sea surface). The atmospheric and external geophysical effects are described in detail by Chelton (1988). The components of height measurement error that are least understood are the instrumental effects. These are all related to the technique by which the range from the satellite to mean sea level is estimated onboard the satellite from the signal received by the altimeter. Though well understood by radar engineers (e.g., Vakman 1968; Caputi 1971), application of the measurement technique to satellite altimetry has not been documented in any easily accessible publication. An understanding of the technical aspects of radar altimetry is crucial to understanding the total error budget for the height measurements.

Altimeter range measurements are generally described in terms of pulse-limited altimetry, which is based on transmitting a short pulse of a few ns duration with relatively broad beamwidth (typically 1°–2°). In the usual description, the power of the pulse reflected from the sea surface is measured as a function of time at intervals of a few ns. The return from spatially averaged sea level at satellite nadir (referred to as "mean sea level") can be uniquely associated with a particular point in the time history of returned power (the so-called "return waveform"). The two-way travel time (equivalent to range after correcting for atmospheric refraction as summarized in Chelton 1988) from the satellite to nadir mean sea level is determined by tracking of this point on the return waveform.

Though it is convenient to think conceptually of radar altimetry in these terms, the actual technique used is quite different. The altimeter transmits a relatively long duration pulse (order μs or ms) and analyzes the returned signal in a way that is effectively equivalent to transmitting a short pulse of a few ns duration. The GEOS-3 altimeter used an actual pulse-compression technique to expand a short pulse for transmission and compress it on receipt using dispersive filters. Subsequent altimeters used a very different technique of extracting equivalent information from a long transmitted pulse without actual expansion or compression of the pulse. The technique is also referred to as "pulse-compression," although the term is a misnomer since a short duration pulse never actually exists at any stage in the receiver. We present here a summary of this pulse-compression technique for analyzing long pulses, a discussion of the method used onboard satellite altimeters to track nadir mean sea level in the returned signal, and discussions of onboard tracking-related instrumental errors in the range measurements. A glossary of symbols used in the text is included in appendix B.

2. Beamwidth-limited and pulse-limited altimetry

The footprint of a narrow-beam radar altimeter is the region on the sea surface illuminated by the antenna beam angle defined by the half power point of the antenna gain pattern. For altimetric measurements of sea surface elevation, the antenna beamwidth should be relatively wide so that the footprint is large enough to filter out the effects of waves on the sea surface, thus obtaining a measure of mean sea level. At the same time, the footprint should be small enough to yield a meaningful measure of mean sea level (i.e., smaller than the Rossby radius of deformation, which is order 50 km). Moreover, a broad beamwidth results in contamination of the measurement when land is present in the side lobes of the antenna pattern. A reasonable compromise is to design the altimeter so that the footprint diameter is a few km.

From an altitude of 1000 km, an altimeter footprint with 5 km diameter could be achieved with an antenna beamwidth of about 0.3°. A beamwidth this narrow requires a large antenna diameter of about 5 m for a 13.6 GHz transmitted signal. An even more stringent limitation of a beamwidth-limited altimeter design is that the accuracy of the measurement of range from the satellite to the sea surface is very sensitive to antenna pointing errors (Fig. 1a). For example, from an altitude of 1000 km, a pointing error γ of only 0.04° corresponds to a range measurement along the antenna boresight (the heavy line in Fig. 1a) that differs from the true altitude (dashed line) by approximately 20 cm. Errors of this magnitude are unacceptably large for oceanographic applications of satellite altimetry. The range error would have to be corrected from the measured antenna pointing angle. It is extremely difficult, however, to measure the pointing angle with this degree of accuracy.

The limitations of a beamwidth-limited altimeter design can be eliminated by using a relatively wide

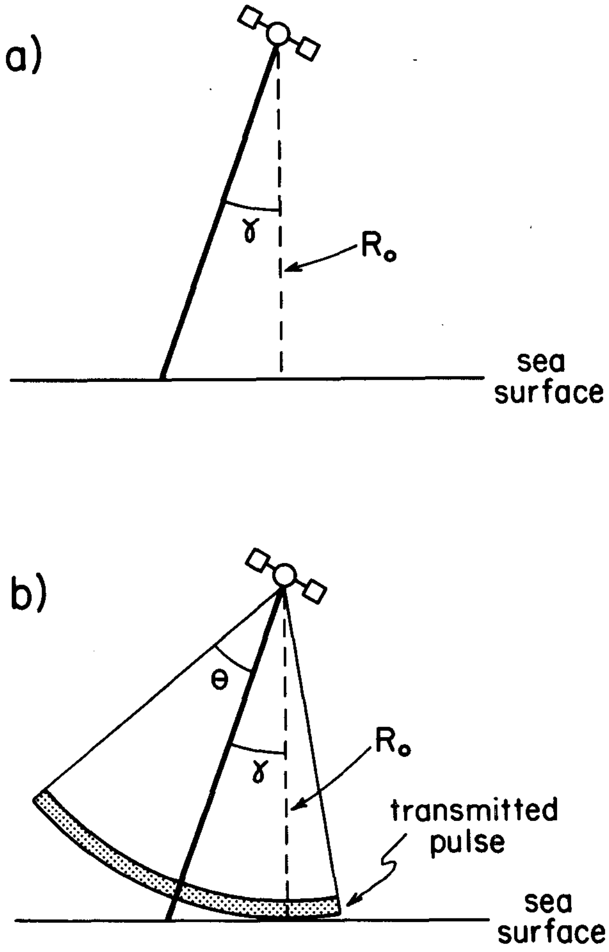

FIG. 1. Measurement geometry for (a) a beamwidth-limited altimeter; and (b) a pulse-limited altimeter. The range R_0 to nadir mean sea level is shown as the dashed line and γ is the antenna pointing angle. The range to mean sea level along the antenna boresight is shown as a heavy line from the satellite to the sea surface.

antenna beamwidth (1°–2°, corresponding to an antenna diameter smaller than 1 m for a 13.6 GHz transmitted signal) and a very short duration transmitted pulse (Fig. 1b). Since the pulse expands spherically as it propagates from the satellite to the sea surface, the travel time for the short pulse to reach satellite nadir is independent of γ. Therefore, as long as the pointing angle γ does not exceed the half beamwidth angle θ of the antenna, the range measurement is relatively insensitive to the antenna pointing angle. (There are, however, corrections that must be applied for off-nadir pointing angle to account for the combined effects of antenna gain pattern and the pulse compression method used to estimate the two-way travel time of the pulse, as discussed in later sections.)

The effective footprint area of the return signal measured by a pulse-limited altimeter can be controlled by the pulse duration. Consider a transmitted pulse with effective duration τ incident on a calm sea surface. (The actual long duration transmitted signal is compressed to a short effective duration by the technique described in section 3. For the discussion in this section, the compressed pulse duration is denoted as τ, though it should be kept in mind that τ refers to the duration of the uncompressed signal in later sections.) This corresponds to a pulse length from leading edge to trailing edge of $c\tau$, where c is the speed of light. The geometry for a spherically expanding short pulse incident on the sea surface is shown in Fig. 2. After the leading edge of the pulse strikes the sea surface, the area illuminated by the pulse becomes a circle that expands with time until the trailing edge of the pulse reaches the calm sea surface a time τ later. Thereafter, the area illuminated by the short pulse becomes an expanding annulus (Fig. 2).

The area of the circular footprint contributing to the signal received by the altimeter can be determined from the altitude R_0 of the satellite above the nadir point and the slant range from the satellite to the outer perimeter of the circle. The two-way slant range for the signal received by the altimeter at time Δt is $2R_0 + c\Delta t$, where Δt is measured relative to the time when the leading edge of the pulse reflected from satellite nadir is received by the altimeter. It is shown in appendix A that the area on the sea surface contributing to the radar return for time $\Delta t < \tau$ is

$$A_{\text{out}}(\Delta t) = \frac{\pi R_0 c \Delta t}{1 + R_0/R_e}, \tag{1}$$

where R_e is the radius of the earth. The denominator in (1) is a correction for the curvature of the earth's surface. The area of the circular footprint thus grows linearly with time (see bottom of Fig. 2).

The area of the circular footprint contributing to the signal received by the altimeter at time τ is

$$A_{\max} = \frac{\pi R_0 c \tau}{1 + R_0/R_e}. \tag{2a}$$

After time τ, the area defined by the outer boundary of the annulus contributing to the radar return continues to grow linearly with time according to (1). The area within the inner boundary of the annulus after time τ is given by

$$A_{\text{in}}(\Delta t) = \frac{\pi R_0 c(\Delta t - \tau)}{1 + R_0/R_e}, \tag{3}$$

which grows linearly from the time when the trailing edge of the pulse reflected from satellite nadir is received by the altimeter. The total area of the annulus is given by

$$\begin{aligned} A_{\text{ann}} &= A_{\text{out}} - A_{\text{in}} \\ &= \frac{\pi R_0 c \tau}{1 + R_0/R_e} \\ &= A_{\max}. \end{aligned} \tag{4}$$

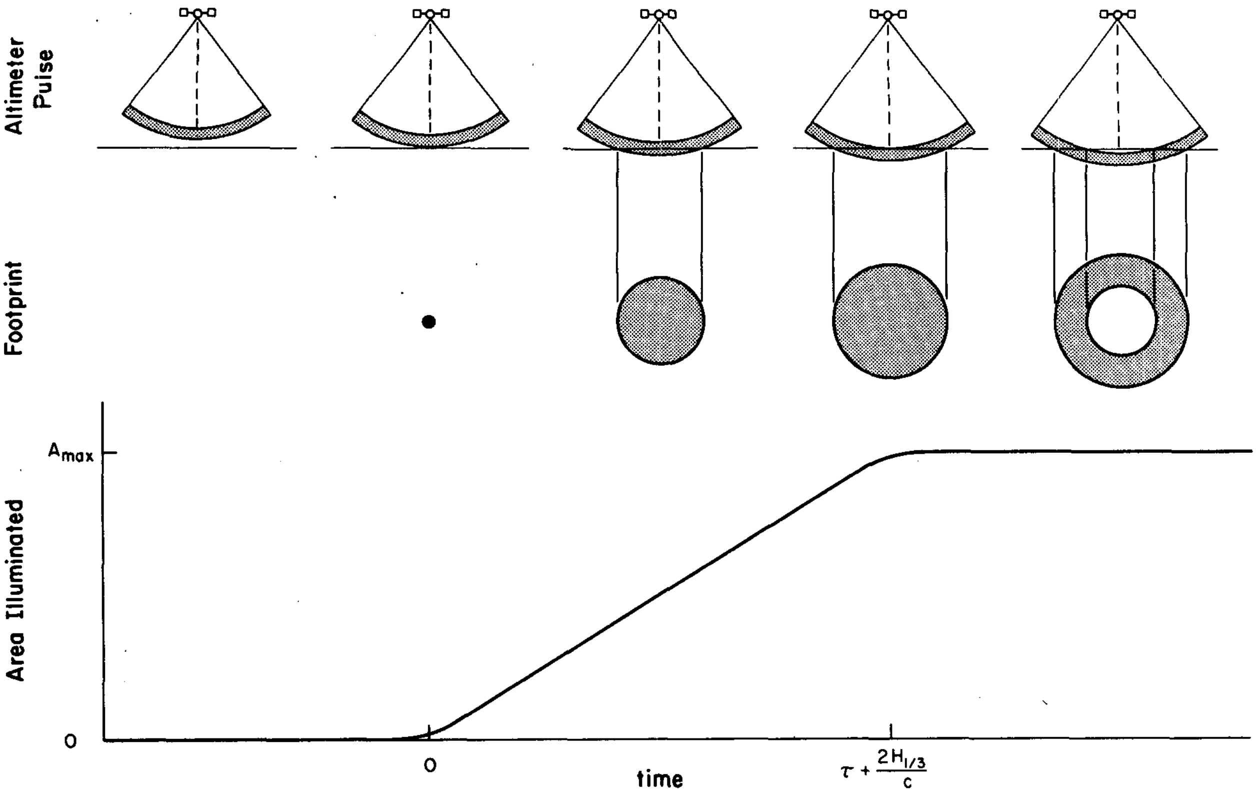

FIG. 2. Schematic representation of a wide beamwidth, short pulse propagating from the satellite to the sea surface (upper row). The footprint on the sea surface contributing to the radar return is shown as a function of time in the middle row. The area of the footprint contributing to the radar return is shown as a function of time in the bottom panel. For a calm sea surface, the area rise time is equal to the compressed effective pulse duration τ (see text). For a rough sea surface with significant wave height $H_{1/3}$, this rise time increases by amount $2c^{-1}H_{1/3}$.

It is evident from (4) that the footprint area contributing to the radar return remains constant after the trailing edge of the short pulse returns from the calm sea surface at satellite nadir (Fig. 2).

The maximum footprint area on a calm sea surface corresponding to (2a) thus depends only on the effective pulse duration and the satellite altitude R_0. Any desired footprint area can be achieved by adjusting the effective pulse duration appropiately. The SEASAT, GEOSAT, and TOPEX altimeters all use an effective pulse duration of 3.125 ns. From the SEASAT and GEOSAT altitudes of 800 km, this gives a spherical earth footprint area A_{max} = 2.09 km^2 on a calm sea surface, which corresponds to an effective footprint diameter of 1.6 km. From the higher 1335 km TOPEX altitude, the footprint area and effective diameter on a calm sea surface increase to 3.25 km^2 and 2.0 km.

The presence of waves increases the area on the sea surface contributing to the radar return. After the leading edge of the altimeter pulse strikes the wave crests on the sea surface at satellite nadir, the footprint becomes an expanding circle. The area of the circular footprint increases linearly with time until the trailing edge of the pulse reaches the wave troughs at satellite nadir (Fig. 3). Thereafter, the footprint becomes an annulus with constant area. Wave conditions are generally characterized by the significant wave height (SWH), defined as four times the standard deviation

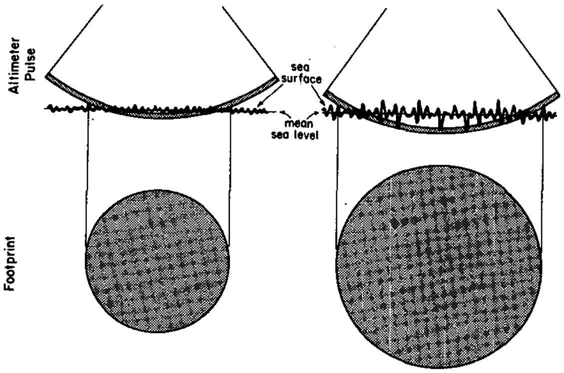

FIG. 3. Schematic representation of a wide beamwidth, short pulse incident on a sea surface with small (left) and large (right) wave heights. The oceanographic footprints corresponding to the time when the trailing edge of the pulse leaves the wave troughs at satellite nadir are shown in the bottom panels. Thereafter, the oceanographic footprint becomes an annulus with constant area.

of the sea surface elevation. SWH corresponds approximately to the crest-to-trough height of the ⅓ largest waves in the footprint and is generally denoted by $H_{1/3}$.

For a wave height $H_{1/3}$, the travel time for the trailing edge of the pulse to propagate from wave crest to trough is $c^{-1}H_{1/3}$. Accounting for two-way travel time, the total rise time for the altimeter footprint area contributing to the radar return from a rough sea surface is therefore $\tau + 2c^{-1}H_{1/3}$ (see Fig. 2). The maximum footprint area contributing to the radar return when the expanding circle becomes an annulus then becomes

$$A_{\max} = \frac{\pi R_0(c\tau + 2H_{1/3})}{1 + R_0/R_e}. \tag{2b}$$

Thereafter, the footprint area is constant. The maximum footprint area contributing to the radar return thus increases linearly with SWH (Fig. 3). The effective footprint diameters computed from (2b) for satellite altitudes of 800 km and 1335 km are given in Table 1 for several values of SWH. From the SEASAT and GEOSAT altitudes of 800 km, the effective footprint diameter increases from 1.6 km for a calm sea surface to 10.8 km for a SWH of 20 m. From the TOPEX altitude of 1335 km, the effective footprint size increases from 2.0 km to 13.4 km for the same range of SWH.

A distinction must be made between "oceanographic footprint", defined to be the total area mapped out by the altimeter footprint, and the pulse-limited area on the sea surface actually illuminated by the radar pulse. The oceanographic footprint described by (2b) defines the area over which spatially averaged sea level is estimated by the altimeter. The diameter of the oceanographic footprint increases with $H_{1/3}$ as summarized in Table 1. It is evident from Fig. 3 that the sea surface within the oceanographic footprint is only sparsely illuminated due to the presence of waves. There are regions within the vertically distributed sea surface that are not within the spherical shell of the short transmitted pulse. The actual pulse-limited sea surface area reflecting the radar pulse is given by (2a), independent of $H_{1/3}$.

TABLE 1. Altimeter antenna effective footprint diameters as a function of significant wave height $H_{1/3}$ computed from (2b) for satellite altitudes of 800 km and 1335 km.

$H_{1/3}$ (m)	Effective footprint diameter (800 km altitude) (km)	Effective footprint diameter (1335 km altitude) (km)
0	1.6	2.0
1	2.9	3.6
3	4.4	5.5
5	5.6	6.9
10	7.7	9.6
15	9.4	11.7
20	10.8	13.4

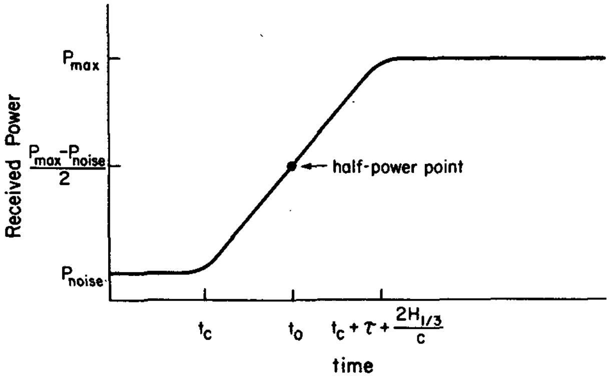

FIG. 4. Power received by a satellite altimeter as a function of time. The background noise power is P_{noise} and the maximum received power (signal plus noise) is $P_{\max}$. The two-way travel time for the leading edge of the pulse to propagate from the satellite to the wave crests and back is t_C. For a calm sea surface, the power rise time is the compressed effective pulse duration τ. For a rough sea surface with significant wave height $H_{1/3}$, this rise time increases by amount $2c^{-1}H_{1/3}$.

From the radar equation [see (43) in appendix A], the power received by a radar antenna is proportional to the area on the sea surface contributing to the radar return. The return power measured by a pulse-limited altimeter is shown as a function of time in Fig. 4. The two-way travel time for the leading edge of the pulse to reflect from the wave crests is t_C. The two-way travel time for the trailing edge of the pulse to reflect from the wave troughs is $t_C + \tau + 2c^{-1}H_{1/3}$. In the "plateau region" after the rise time $\tau + 2c^{-1}H_{1/3}$ in the power time series, the returned power for a real antenna will actually decrease due to the rolloff of the antenna gain pattern (see further discussion in section 3a).

The power time series shown schematically in Fig. 4 is referred to as the return waveform. Mean sea level corresponds to half the distance between wave crests and troughs. In this case, the two-way travel time t_0 for the center of the pulse (midway between the leading and trailing edges) to reflect from mean sea level is $t_C + \tau/2 + c^{-1}H_{1/3}$, which corresponds to the point on the return waveform where the power is half of the difference between $P_{\max}$ and the background noise power P_{noise}. The slope of the return waveform near the half-power point of the leading edge is $(P_{\max} - P_{\text{noise}})/(\tau + 2c^{-1}H_{1/3})$. Thus, the two-way travel time, and hence the range to mean sea level, can be determined by tracking the half-power point on the return waveform. In addition, SWH can be determined from the slope of the leading edge of the waveform in the vicinity of the half-power point.

3. Pulse compression

From the discussion in the preceding section, the pulse-limited altimeter design can be used to determine SWH and the range from the satellite to mean sea level from the time history of the return power. The footprint area depends on the pulse duration and SWH within the altimeter footprint according to (2b). An effective pulse duration of 3.125 ns results in an effective oceanographic footprint diameter that increases from a few km for calm seas to 10–15 km for very large wave heights (Table 1). It is difficult to generate a pulse length this short with sufficient power to insure adequate signal-to-noise ratio. In practice, a pulse-compression technique is used to obtain equivalent information from a relatively long pulse with order μs or ms duration. The longer pulse greatly improves the signal-to-noise ratio in the altimetric measurements. The method used to extract from a long pulse a return waveform analogous to Fig. 4 is described in section 3a. Digital sampling of the waveform to obtain the equivalent of a discrete time series of returned power is described in section 3b.

a. Spectral waveforms

The technique of pulse compression is based upon transmitting a "chirp" consisting of a ramp signal with linear frequency change ΔF over a sweep period τ, as shown schematically in Fig. 5. For SEASAT, a dispersive wave device was used to generate the chirp. At that time, these devices were limited to a time-bandwidth product of a few hundred; the sweep time τ was 3.2 μs, the center frequency F_0 of the chirp was 13.5 GHz, and the chirp frequency range ΔF was 320 MHz. Beginning with GEOSAT, a digital chirp generation technique was used which allowed a longer sweep period. The same system will be used on TOPEX. The GEOSAT and TOPEX chirp sweep times τ are 102.4 μs, with the same frequency range ΔF = 320 MHz. GEOSAT incorporates the same 13.5 GHz center frequency as SEASAT. TOPEX will incorporate a dual-frequency altimeter with center frequencies 13.6 and 5.3 GHz. Since the ionospheric range delay is inversely proportional to the square of the transmitted frequency, the TOPEX altimetric measurements at two frequencies allow simultaneous estimates of the vertically integrated ionospheric electron content and the range to mean sea level corrected for ionospheric range delays (Chelton 1988).

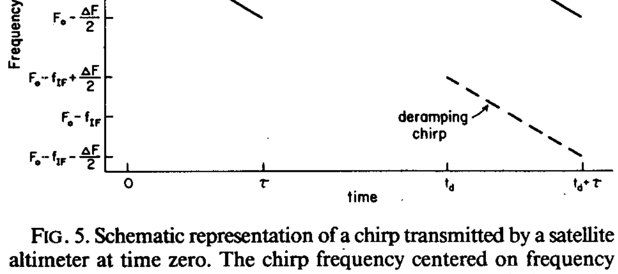

FIG. 5. Schematic representation of a chirp transmitted by a satellite altimeter at time zero. The chirp frequency centered on frequency F_0 decreases linearly by amount ΔF over the sweep period τ. A deramping chirp (dashed line) is generated internally by the altimeter at time t_d, which is intended to match the arrival time of the reflected chirp from nadir mean sea level. The deramping chirp is identical to the transmitted chirp, but with frequency lower by amount f_{IF}.

Radar receivers generally pass the returned signal through a low-noise amplifier and mix it with a locally generated signal with nearly the same frequency. An intermediate frequency (IF) signal with frequency equal to the difference between the received and locally generated signals is produced. For the high range-resolution radars under consideration here (the SEASAT, GEOSAT, and TOPEX altimeters), the IF signal is centered at 500 MHz. The IF signal provides a convenient point in the signal processing to apply automatic gain control attenuation (see section 4).

In pulse compression, the altimeter hardware generates internally a "deramping" chirp at time lag t_d after the transmitted pulse (Fig. 5). The deramping chirp is identical to the transmitted chirp except that the center frequency differs from that of the transmitted chirp by an amount equal to the desired IF frequency f_{IF}. If the time lag t_d between transmitted and deramping chirps is properly timed to match the arrival time of the reflected chirp from nadir mean sea level as shown in Fig. 5, then t_d is the two-way travel time from the altimeter to mean sea level. With appropriate corrections for atmospheric refraction (Chelton 1988), this can be converted to the range between the altimeter and mean sea level.

The returned and deramping chirps are mixed together and the difference frequency is the IF signal that is to be processed. This is shown schematically in Fig. 6 for a very narrow beamwidth chirp returned from a calm sea surface at time t_0. If the altimeter generates the deramping chirp a time Δt_d earlier (later) than the time t_0 of the return signal, then the frequency of the IF signal will be higher (lower) than the nominal value f_{IF} by an amount

$$\Delta f' = Q\Delta t_d, \tag{5}$$

where $Q = \Delta F/\tau$ is the sweep rate of the chirp and $\Delta t_d = t_0 - t_d$. The nonoverlapping portions of the actual deramping chirp and the returned chirp are not included in subsequent processing. As long as the timing error Δt_d is small, this is a small portion of the total chirp length τ so that the total record length of the IF signal to be processed is $\tau - \Delta t_d \approx \tau$.

Although there is no advantage to a long chirp over a short one as far as travel-time resolution is concerned (for fixed ΔF), the long pulse improves the radar signal-to-noise ratio. All radar systems are plagued by internally generated thermal white noise. Since the power of this white noise is uniformly distributed with frequency, the total noise power is proportional to the bandwidth ΔF of the receiver, independent of the pulse duration. However, increasing the pulse duration increases the total transmitted signal energy, thus im-

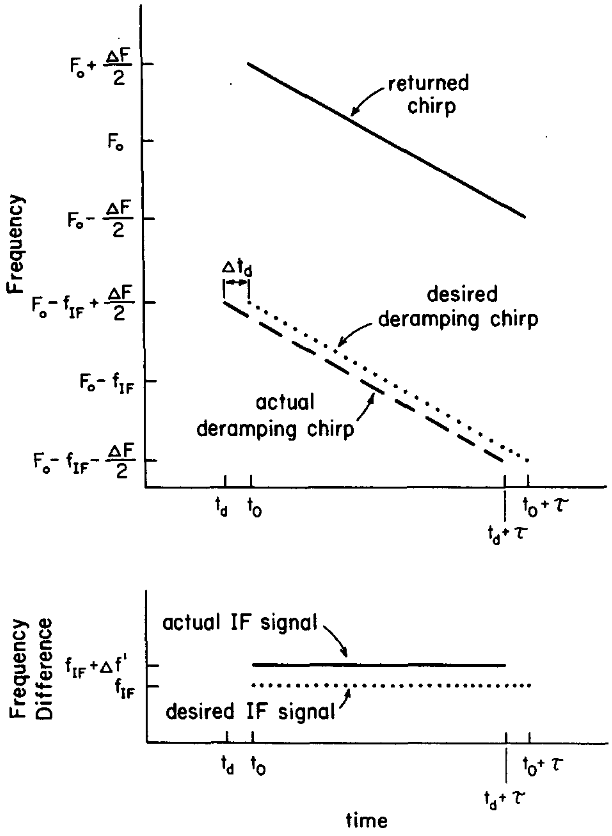

FIG. 6. Upper: Schematic representation of a very narrow beamwidth chirp returned from a smooth sea surface at time t_0 (solid line) and a deramping chirp (dashed line) generated internally by the altimeter at time t_d. Lower: The difference between the deramping chirp and returned chirp. The desired deramping chirp and corresponding IF signal are shown by the dotted lines. The actual deramping chirp generated a time $\Delta t_d = t_0 - t_d$ before the returned chirp is received is shown by the dashed line. The corresponding actual IF signal is shown as a solid line in the lower panel.

proving the signal-to-noise ratio (Skolnik 1970, section 2). The digital chirp generation technique allowing a chirp length 32 times longer for GEOSAT and TOPEX than for SEASAT could result in an increased signal-to-noise ratio. Alternatively, the increased signal energy from a longer pulse duration could be offset by transmitting with lower power, achieving about the same signal-to-noise ratio. This latter option has been adopted for both GEOSAT and TOPEX. The GEOS-3 and SEASAT altimeters used a travelling wave tube (TWT) amplifier which transmitted a peak signal power of 2 kW. Evidence indicates that these amplifiers could support only a few thousand hours of useful operation. GEOSAT and the TOPEX 13.6 GHz altimeter also incorporate TWT amplifiers, but with only 20 W peak power, which should have considerably longer lifetimes. In addition to pulse length and transmitted power, the signal-to-noise ratio is also determined by the antenna beamwidth (1.6° for SEASAT, 2.1° for GEOSAT, and 1.1° for TOPEX) and satellite altitude (800 km for SEASAT and GEOSAT, 1335 km for TOPEX). The signal-to-noise ratio decreases with increasing antenna beamwidth and satellite altitude. The end result is that the signal-to-noise ratios are comparable for SEASAT and TOPEX, and somewhat lower for GEOSAT. With the lower power requirement of a longer pulse duration, it also becomes possible to replace the conventional TWT amplifier design with more reliable solid state electronics. The TOPEX 5.3 GHz altimeter and the POSEIDON altimeter will be the first to use solid state amplifiers, transmitting with peak powers of 20 W and 3.5 W, respectively.

The deramping chirp must be generated at exactly the time when the transmitted chirp returns from mean sea level at satellite nadir to obtain an accurate measure of the height of the satellite above the sea surface. This delay is set by the adaptive tracking unit (ATU), as described in section 4. We first describe the nature of the signal analyzed by the ATU. Consider an altimeter pulse with extremely narrow beamwidth incident on a rough sea surface. This will later be generalized to a more realistic broad beamwidth. From (5), the frequency deviation $\Delta f'$ from the nominal frequency $f_{\rm IF}$ clearly depends on the error Δt_d in the delay between the transmitted and deramping chirps. The backscatter from the sea surface near satellite nadir is governed by geometric optics. Within the altimeter footprint, there are many wave facets on the rough sea surface oriented perpendicular to the incident radiation. Thus, the signal returned to the altimeter consists of a superposition of specularly reflected pulses from many points on the sea surface.

For the sake of clarity, suppose for the moment that there are only three reflecting wave facets in the small nadir footprint of this very narrow beamwidth altimeter as shown in Fig. 7: one at a wave crest, one at mean sea level, and one at a wave trough (respectively denoted by C, 0, and T). Then there would be three returned chirps, one from each reflecting surface (Fig. 8). The chirp returned from the wave crest would be received first by the altimeter. The chirp returned from the wave trough would be received last. The tracker generates the deramping chirp at the time it expects the reflected chirp from nadir mean sea level. This time is estimated from previous measurements as described in section 4. The IF signals obtained by differencing the three returned chirps (see Fig. 8) with the deramping chirp have frequencies given by

$$\begin{aligned} f_0 &= f_{\rm IF} + Q\Delta t_d \\ f_C &= f_0 - Q(t_0 - t_C) \\ f_T &= f_0 + Q(t_T - t_0), \end{aligned} \tag{6}$$

where t_C, t_0, and t_T are the arrival times of the returned chirps from the wave crest, mean sea level, and the wave trough, and Δt_d is the ATU error in estimating

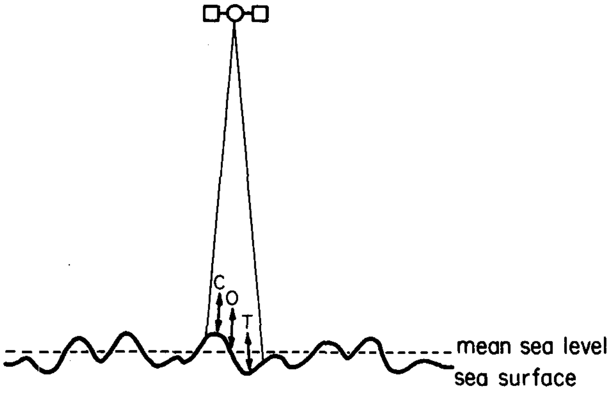

FIG. 7. Idealized representation of a very narrow beamwidth antenna with only three reflecting wave facets in the antenna beamwidth (C located at a wave crest, 0 located at mean sea level, and T located at a wave trough).

the arrival time of the signal returned from mean sea level (shown as zero in Fig. 8). The (positive) time differences ($t_0 - t_C$) and ($t_T - t_0$) depend on the sea surface wave height. Note that $f_C < f_0 < f_T$, i.e., the frequency of the signal scattered from the wave crest is lower, and the frequency of the signal scattered from the wave trough is higher than that scattered from mean sea level. Also note the important point that the frequency relative to f_0 is linearly proportional to the two-way travel time difference relative to mean sea level. Thus, frequency and travel time (equivalent to the range from the satellite to the reflecting point on the sea surface) are linearly related. A two-way travel time difference Δt relative to t_0 corresponds to a frequency difference Δf relative to f_0 of

$$\Delta f = Q\Delta t. \qquad (7)$$

The total returned signal received by the altimeter in this simple example is the sum of the three returned chirps. Since the three wave facets oriented perpendicular to the incident radiation reflect with equal efficiency, the total IF signal obtained by differencing the total received signal and the deramping chirp in this example has equal power at the three frequencies f_C, f_0, f_T. The spectrum P_3 of the returned signal is therefore three line spectra as shown in Fig. 9a. (In actual practice, these line spectra would be smeared as approximately $[\sin(\pi f\tau)/(\pi f\tau)]^2$ due to the finite record length τ of the IF signal.)

The above results can now be generalized to the case of a sea surface with a continuous distribution of reflecting surfaces (but still a very narrow antenna beamwidth). The total received signal is the sum of the returned chirps from all specularly reflecting points on the sea surface. The shape of the frequency distribution of the power of the returned signal is therefore very nearly the same as that of the sea surface height distribution. For a Gaussian sea surface height distribution, the distribution of surface reflectors is, to first order, also Gaussian. The spectrum $P(f)$ of the signal returned from a small area on the sea surface with a Gaussian sea surface height distribution is therefore approximately Gaussian, as shown in Fig. 9b. The peak of the spectrum is at the frequency f_0 of the radar return from nadir mean sea level. The width of the Gaussian distribution is directly related to the standard deviation of sea surface height.

The above description was for an altimeter with very narrow beamwidth. These results can now be generalized to the case of a realistic broad antenna beamwidth (typically 1°–2°). The chirp of duration τ transmitted by the altimeter radiates as a spherically expanding pulse. It is assumed that the sea surface height distribution is homogeneous over the altimeter footprint within the antenna beamwidth. The time required for the pulse to travel to a point on the sea surface and back to the altimeter depends on the angle θ_L relative to antenna boresight, or equivalently the distance L from satellite nadir to the point on the sea surface (Fig.

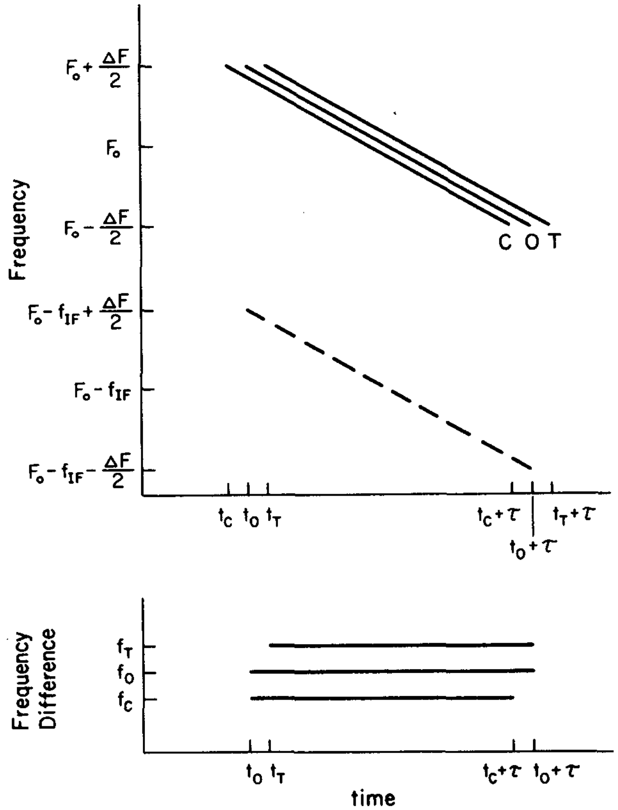

FIG. 8. Upper: Schematic representation of chirps returned from the three points on the sea surface shown in Fig. 7 (a wave crest C, mean sea level 0, and a wave trough T). Dashed line represents a deramping chirp as in Fig. 6 generated at the time t_0 that the return from mean sea level is received. Lower: The differences between the deramping chirp and the three reflected chirps. The frequencies of these three IF signals are given by (6).

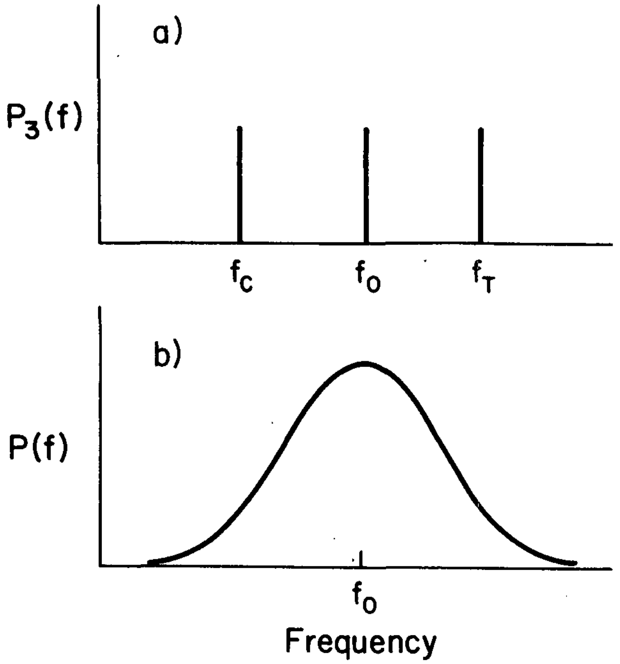

FIG. 9. Power spectrum of the total returned IF signal for a very narrow beamwidth antenna. The idealized case of only three reflecting wave facets, as shown in Figs. 7 and 8, is shown as $P_3(f)$ in (a). A more realistic case of a Gaussian distribution of sea surface height (and surface reflectors), but still a very narrow antenna beamwidth, is shown as $P(f)$ in (b). The frequency f_0 corresponds to the frequency of the IF signal from mean sea level.

10). From any small area on the sea surface, the power of the IF signal obtained by differencing the received signal and the deramping chirp will be approximately Gaussian, as shown in Fig. 9b for a very narrow antenna beamwidth. For a broad beamwidth, the time delay between the signal reflected from a small area on the sea surface increases with increasing distance L from satellite nadir. Let R_0 be the range from the satellite to nadir mean sea level. The range R_L from the satellite to mean sea level an arc length L from nadir on a spherical earth, corresponding to angle θ_L relative to the antenna boresight, is

$$R_L = R_0 + \Delta r_L, \tag{8}$$

where Δr_L is the range difference to mean sea level at L compared with the range to nadir mean sea level. (The distances L, R_L, and Δr_L are referred to as L', R'_L, and $\Delta r'_L$, respectively, in section A3 to distinguish them from flat-earth approximations; the primes have been dropped here for convenience.) The differential range shown in section A3 to be

$$\Delta r_L \approx \frac{R_0 \theta_L{}^2}{2}(1 + R_0/R_e). \tag{9}$$

The term in parentheses is a 10%–20% correction (depending on R_0) to account for the curvature of the earth. The ranges R_0, R_L and Δr_L can all be expressed equivalently as time. Accounting for two-way travel of the radar pulse from the satellite to the sea surface and back, the travel times for speed of light c are

$$t_0 = 2R_0/c$$

$$t_L = 2R_L/c$$

$$\Delta t_L = t_L - t_0 = \frac{2\Delta r_L}{c} = \frac{R_0\theta_L{}^2}{c}(1 + R_0/R_e). \tag{10}$$

(The differential travel time Δt_L is referred to as $\Delta t'_L$ in appendix A to distinguish it from a flat-earth approximation; the prime is dropped here for convenience.) The differential two-way travel times thus increase approximately quadratically with increasing angle θ_L.

From the previously discussed special case of a very narrow beamwidth antenna, the spectrum of power returned from any small region on the sea surface is approximately Gaussian. For a small area on the sea surface a distance L from satellite nadir, the center frequency of the Gaussian spectrum is f_L, corresponding to the frequency of the chirp backscattered from mean sea level at L. Since the frequency of the IF signal obtained by differencing the deramping chirp and returned chirp increases linearly with two-way travel time according to (7), the frequency f_L is given by

$$\begin{aligned} f_L &= f_0 + Q\Delta t_L \\ &= f_0 + \frac{QR_0\theta_L{}^2}{c}(1 + R_0/R_e), \end{aligned} \tag{11}$$

where $f_0 = f_{\text{IF}} + Q\Delta t_d$ is the frequency of the chirp reflected from nadir mean sea level for an error Δt_d in the timing of the deramping chirp.

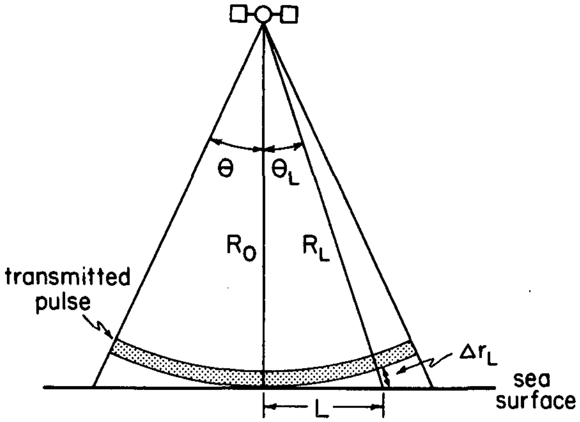

FIG. 10. Schematic diagram of a satellite altimeter with antenna half beamwidth θ. The height of the satellite above the nadir point is R_0, and the range from the satellite to a point on the sea surface a distance L from nadir (corresponding to antenna angle θ_L) is R_L. The range difference Δr_L is equal to $(R_L - R_0)$.

The total signal returned to the satellite is the sum of the signals returned from all favorably oriented wave facets in the altimeter footprint. If the antenna gain were one across the entire broad antenna beamwidth, the spectrum of the total IF signal would be as shown in Fig. 11a. Mathematically, this is given by a convolution of the spectrum $P(f)$ of the deramped IF signal for a very narrow antenna beamwidth (Fig. 9b) with a Heaviside step function $H(f-f_0)$ which has value 0 for $f<f_0$ and 1 for $f \geqslant f_0$ (thus integrating the return from satellite nadir, where the center frequency is f_0, to higher antenna angles),

$$S_1(f)=P(f)*H(f-f_0)=\int_{f_0}^{\infty} P(f-u)du. \quad (12)$$

The spectral energy of course must eventually decrease to zero since the antenna beamwidth is finite, but this effect has been ignored in this idealized case. Recall that the shape of $P(f)$ is the same as that of the sea surface height distribution, which is approximately Gaussian. The total "spectral waveform" returned from the sea surface for this idealized broad beamwidth antenna therefore has approximately the shape of an error function. Note that the frequency f_0 corresponding to the return from nadir mean sea level is at the half-power point if the sea surface height distribution is symmetric (e.g., Gaussian). The slope of the leading edge of the spectral waveform decreases with increasing sea surface height standard deviation (or equivalently the SWH), but the location of the half-power point is not sensitive to the height standard deviation.

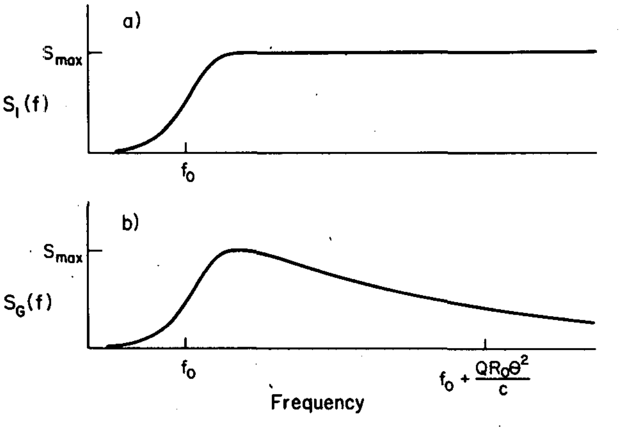

FIG. 11. Power spectrum of returned signal from the sea surface for a broad antenna beamwidth for (a) the idealized case (12) of gain of 1 across a wide beamwidth antenna, and (b) a realistic case (13) of antenna gain pattern $G(\theta_L)$ with half beamwidth θ. The frequency f_0 corresponds to the signal reflected from mean sea level at nadir and has half the maximum power of the spectral waveform. The frequency $f_0+QR_0\theta^2/c$ corresponds to the signal reflected from mean sea level on a flat earth at the half-power angle θ of the antenna beamwidth. For a spherical earth, this frequency must be multiplied by $1+R_0/R_e$, as in (11).

The spectral waveform (12) is analogous to the time history of power received by a pulse-limited altimeter as shown in Fig. 4. The important difference is that the abscissa in Fig. 4 is time, while the abscissa in Fig. 11a is frequency. Since two-way travel time and frequency in the IF signal are directly related by (7), the frequency and time domain representations in Figs. 11a and 4 are equivalent. Thus, differencing the return signal with a deramping chirp "compresses" a long duration pulse to obtain information equivalent to that which can be obtained from a very short pulse.

For the more general case of an antenna with realistic gain pattern and half-power point at angle θ, the spectrum of the total IF signal is a convolution of the sea surface height distribution with the antenna gain, as shown in Fig. 11b. The angle θ_L relative to the antenna boresight and the frequency of the IF signal are directly related by (11). The antenna gain $G(\theta_L)$ can therefore be expressed equivalently in terms of frequency as $G(f)$ (see section A3). The spectrum of the total IF signal is then given mathematically by the convolution

$$S_G(f)=P(f)*G(f)=\int_{f_0}^{\infty} P(f-u)G(u)du. \quad (13)$$

The effect of the gain pattern is to decrease the power in the plateau region of the spectral waveform. Typical antenna gain patterns are approximately Gaussian for small angles θ_L. It is shown in section A3 that the antenna gain for nadir pointing angle can be expressed as

$$G(f)=\exp\left[-\frac{cg(f_L-f_0)}{QR_0(1+R_0/R_e)}\right] \quad (14)$$

where g is the decay rate of the Gaussian gain pattern. The more general case for off-nadir antenna pointing angle is given by Brown (1977) and Rodriguez (1988). Expressed in terms of frequency, the gain decays approximately exponentially with increasing frequency (see Fig. 11b). Note that a flat-earth approximation to $G(f)$ (equivalent to setting $R_e=\infty$) gives a gain value that is 10%–20% too high, depending on the satellite altitude R_0. The rate of "plateau droop" depends on the antenna beamwidth and the decay factor g of the gain pattern. A narrow beamwidth results in a faster dropoff with increasing frequency in the plateau region.

The formulation (13) for the spectral waveform is for infinite record length of the IF signal. To account for the effects of finite record length τ, the spectrum $S_G(f)$ must be convolved with a spectral window given approximately by $[\tau \sin(\pi f\tau)/(\pi f\tau)]^2$. This spectral window is generally referred to as the "point target response". This smearing of the spectral waveform due to finite record length limits the two-way travel time resolution of the altimeter. The frequency bandwidth of the center lobe of the spectral window is $1/\tau$. From

(7), this frequency bandwidth corresponds to a two-way travel time resolution of $1/\Delta F$. Since ΔF is 320 MHz for SEASAT, GEOSAT and TOPEX, the travel time resolution (i.e., the effective pulse width) is 3.125 ns for all three altimeters.

It should be pointed out that the smooth spectral waveforms in Fig. 11 exist only in the average of many individual waveforms. Within the altimeter footprint on the sea surface, there will always be many wave facets specularly reflecting the incident signal at a given range. The returned signal from a single wave facet can be expressed as an amplitude and a phase, or equivalently, in terms of real and imaginary components. Since the radar wavelength is short (approximately 2.2 cm for a 13.6 GHz signal), the phase relationships between signals reflected from the various facets is random. The total signal received by the altimeter is the vector addition of the real and imaginary components from all individual specularly oriented wave facets in the altimeter footprint. By the Central Limit Theorem, the real and imaginary components of the total signal are both approximately Gaussian distributed random variables. The amplitude of the total returned signal is therefore Rayleigh-distributed and the returned power (proportional to the square of the amplitude) at each frequency is an exponentially distributed random variable. Since each frequency samples a different collection of wave facets, this geophysical variability results in a noiselike appearance of each individual return waveform.

As the altimeter moves along the satellite orbit, the path lengths to the various facets change. The wave facet phase relationships therefore change and the returned signal amplitude undergoes different Rayleigh fluctuations in each waveform (Ulaby et al. 1988). These fluctuations are sometimes referred to as "Rayleigh fading" of the radar signal. Many individual waveforms must therefore be averaged to obtain a mean waveform with the smooth shape shown in Fig. 11b. If each waveform is statistically independent (which depends on the pulse repetition rate and the satellite orbital velocity), the Rayleigh noise decreases as the square root of the number of waveforms in the average. Walsh (1982) has shown that the maximum pulse repetition rate for independent samples is proportional to the square root of SWH, increasing from about 1000 pulses per second for 2-m wave height to 3000 pulses per second for 10-m wave height for the SEASAT orbit height. Simulated examples of averages of 1, 25, and 1000 independent waveforms are shown in Fig. 12. The simulations are for a Gaussian sea surface height distribution and ideal antenna with uniform gain across the antenna beamwidth as described by (12) and shown in Fig. 11a.

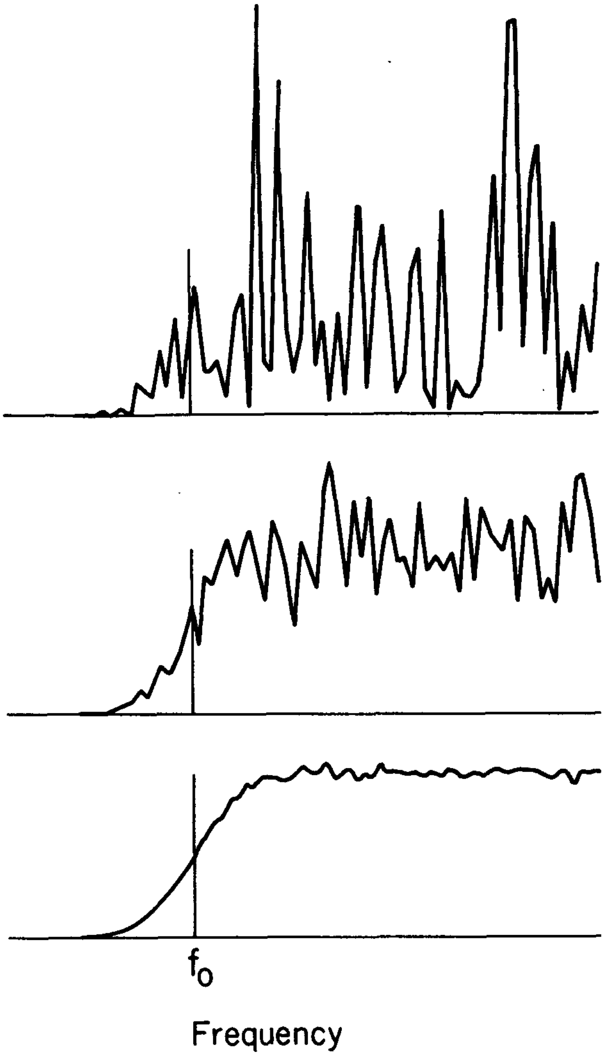

FIG. 12. Averages of 1, 25, and 1000 (top to bottom) simulated altimeter waveforms with realistic Rayleigh-distributed geophysical noise. (After Townsend et al. 1981.)

b. Waveform sampling

It was shown in section 3a that the use of a chirped signal and the deramping technique results in an equivalence between two-way travel time and frequency in the analyzed IF signal as described by (7). To utilize this information, the waveform returned from the sea surface must be spectrally analyzed. The analog spectral waveform is digitally sampled at discrete frequencies for the ATU to determine the shift necessary to keep the return from nadir mean sea level at the half-power point of the leading edge of the waveform as described in section 4. One method of achieving this would be to bandpass-filter the total returned IF signal with a bank of filters and store the spectral power in each band. The disadvantage of this approach is that any inaccuracies in the filter response of each bandpass filter would result in irregularities in the discrete spectral waveform (sampler gain calibration errors, see section 5c), leading to errors in the tracking of mean sea level.

A better method is to sample the spectral waveform digitally in the frequency domain using discrete Fourier transform methods. Recall that the record length of the total IF signal after deramping is approximately equal to the pulse duration τ. The minimum frequency interval that can be resolved by this record length is $\delta f = 1/\tau$. For SEASAT, which used a chirp length $\tau = 3.2$ μs, the frequency resolution δf was 312.5 kHz. For GEOSAT and TOPEX, with chirp lengths of 102.4 μs, the frequency resolution is 9.766 kHz. There is no advantage to sampling the spectral waveform at a frequency interval smaller than δf since this is the minimum interval between independent samples.

The method used to sample the returned waveform at frequency interval δf is to sample the analog received signal at the appropriate interval in the time domain, then compute the discrete Fourier transform (DFT) of the discretely sampled time series. The record length τ can be written as $\tau = N\delta t$, where δt is the sample interval in the time domain and N is the corresponding number of samples. From (7), the effective two-way travel time resolution corresponding to a frequency resolution of δf in the spectral waveform is

$$\delta t_{\text{eff}} = \frac{\delta f}{Q} = \frac{1}{\Delta F}. \qquad (15)$$

Note that δt_{eff} depends only on the chirp frequency range ΔF. Since SEASAT, GEOSAT and TOPEX all use $\Delta F = 320$ MHz, the effective two-way travel time resolution is 3.125 ns for all three systems. This is equivalent to a one-way range resolution of approximately 47 cm in the digitally sampled time series. Sampling the 3.2-μs SEASAT returned signal at intervals of $\delta t = \delta t_{\text{eff}}$ would have resulted in a total of $N = 1024$ samples of each returned pulse. For the longer 102.4 μs GEOSAT and TOPEX pulses, the same sample interval would result in a total of 32 768 samples of each returned pulse.

When discretely sampling an analog time series, care must be taken to avoid aliasing of unresolved high frequency variability. The highest frequency that can be resolved by a sample interval δt is the Nyquist frequency $f_N = 1/(2\delta t)$. Depending on the antenna half beamwidth θ, the IF signal returned from the sea surface (see Fig. 11b) may have significant energy at frequencies higher than f_N. To be certain that no high frequency energy is aliased into the frequencies of interest, the analog returned signal must be low-pass filtered with an "anti-aliasing" filter designed to attenuate frequencies higher than f_N. This filtering must be applied before the time series is digitally sampled.

Sampling the analog received signal of record length τ at intervals of δt in the time domain, and then computing the DFT of the time series gives a discretely sampled waveform in the frequency domain with frequency interval $\delta f = 1/\tau$, as shown schematically by the dots in Fig. 13. Since frequency and two-way travel time are equivalent according to (7), each discretely sampled frequency corresponds to a different two-way travel time (i.e., range). The discretely sampled frequencies are therefore often referred to as "range gates".

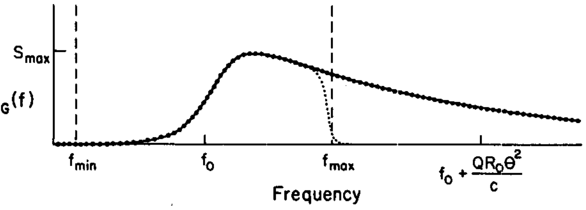

FIG. 13. Schematic representation of a discretely sampled spectral waveform (with samples shown by dots). The frequency f_0 corresponds to the return from nadir mean sea level. Only the portion of the waveform between frequencies f_{min} and f_{max} (bracketed by the vertical dashed lines) is required for waveform processing. The dotted line shows the spectral waveform obtained by low-pass filtering the analog received signal to remove frequencies higher than f_{max}.

The two geophysical quantities to be extracted from the spectral waveform are the range to nadir mean sea level (which should be located at the half-power point of the leading edge of the waveform if the ATU is functioning properly), and SWH (inversely related to the slope of the leading edge of the waveform, as discussed in section 2). Thus, only the portion of the full waveform near the leading edge is required for waveform processing. The important portion of the spectral waveform is bracketed by the dashed lines in Fig. 13. Note that the frequency interval δf depends only on the chirp length τ and not on the sample interval δt. By taking advantage of this reduced frequency range requirement, it is possible to sample the analog received signal at a sample interval δt much larger than $\delta t_{\text{eff}} = 3.125$ ns and still retain the full frequency resolution δf across the restricted frequency range (and hence retaining a two-way travel time resolution of 3.125 ns in the waveform). The anti-aliasing filter must be designed to attenuate frequencies greater than f_{max} (see Fig. 13), thus attenuating most of the trailing edge of the spectral waveform (see dotted line in Fig. 13).

The SEASAT altimeter used a sample interval of $\delta t = 50$ ns, and an anti-aliasing filter with maximum frequency $f_{\text{max}} = f_0 + 10$ MHz = 510 MHz. The increased sample interval corresponded to a reduction from 1024 to 64 in the number of samples N, thus resulting in a significant computational savings in the DFTs applied to sample the waveform at frequency interval δf. The GEOSAT altimeter uses a sample interval of 1.6 μs and an anti-aliasing cutoff frequency of $f_0 + 312.5$ kHz. With the longer 102.4 μs pulse duration, this sample interval and low-pass filtering reduce the number of samples N from 32 768 to 64. TOPEX will sample the IF signal with sample interval 0.8 μs with an anti-aliasing cutoff frequency of $f_0 + 625$ kHz, resulting in a total of $N = 128$ samples of the IF signal.

The SEASAT and GEOSAT altimeters sampled the spectral waveform at 60 contiguous frequencies separated by δf (312.5 kHz for SEASAT and 9.766 kHz for GEOSAT) using the DFT method described above. This bank of 60 DFT range gates was centered on the frequency f_0 (referred to as the track point) corresponding to the return from nadir mean sea level. Three additional interleaved frequencies were sampled near the center point (range gates 29.5, 30.5 and 31.5). With proper tracker function, the half-power point corresponding to the frequency of the IF signal from nadir mean sea level is placed in range gate 30.5, as shown by the example SEASAT waveform in Fig. 14. The sudden drop in power in the last few range gates is due to the band-edge rolloff of the anti-aliasing filter implemented to allow the reduced number of samples in the time domain.

The TOPEX altimeter will use a slightly modified procedure for sampling the spectral waveform. The waveform will be sampled at 128 frequency range gates using fast Fourier transform (FFT) techniques. The half-power track point will be placed between range gates 32 and 33, thus resolving more of the trailing edge of the waveform. The FFT method yields spectral values at uniformly spaced frequencies, and therefore does not lend itself easily to the use of interleaved range gates near the track point (as done with SEASAT and GEOSAT). All of the TOPEX waveform samples will be separated by $\delta f = 9.766$ kHz, corresponding to the same 3.125 ns two-way travel time resolution as SEASAT and GEOSAT (approximately 47 cm in range). With the FFT method, TOPEX waveforms will be sampled at twice as many range gates as SEASAT and GEOSAT in only about $1/8$ of the time of the DFT method.

Because of the linear relation (7) between frequency in spectral waveforms and two-way travel time (and hence range), pulse compression and digital sampling of the waveform at frequency interval δf are equivalent to transmitting a very short pulse and measuring the time history of the return in a sequence of range gates separated by an effective two-way travel time resolution of $\delta t_{\text{eff}} = 3.125$ ns. However, the higher signal power that can be achieved by pulse compression makes it much more practical than actually transmitting a short pulse. The use of an anti-aliasing filter to restrict the frequency content of the IF signal in pulse compression also simplifies altimetry by allowing a time domain sample interval much larger than 3.125 ns, while still achieving a two-way travel time resolution of 3.125 ns in the spectral waveform.

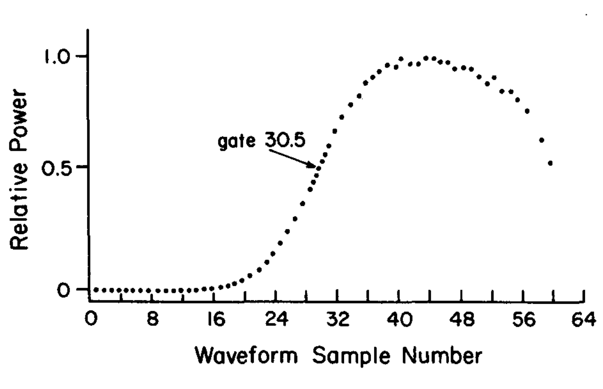

FIG. 14. Example SEASAT waveform (average of 1000) for 11.0 m SWH (after Townsend 1980). The waveform has been normalized to have a maximum value of 1. The dots correspond to the 60 contiguous range gates separated by 3.125 ns, with three additional gates (gates 29.5, 30.5 and 31.5) interleaved near the center of the leading edge of the waveform. The half-power point is placed in gate 30.5 by the adaptive tracking unit.

4. Onboard tracking of mean sea level

The primary objective of satellite altimetry is to estimate the height of the satellite above mean sea level. From section 3, the two-way travel time for the altimeter pulse is equal to the time difference between the transmitted and deramping chirp only if the deramping chirp is properly timed to coincide with the return from nadir mean sea level. With appropriate corrections for atmospheric refraction and altimeter hardware timing delays, range can be determined from the two-way travel time. The techniques of pulse compression and digital sampling of the return waveform have been summarized in section 3. This section summarizes the tracking method used onboard the satellite to analyze the digital waveform and maintain the half-power point in the tracking gate at frequency f_0. Mean sea level can also be estimated using various ground-based waveform processing techniques described in the literature (Lipa and Barrick 1981; Hayne 1981; Srokosz 1986; Rodriguez 1988; Rodriguez and Chapman 1989). The tradeoffs between accuracies of these methods and computational burden compared with the onboard waveform processing technique described here are presently under evaluation.

In order to operate the altimeter electronics within the linear response region of all receiver stages, an automatic gain control (AGC) loop is implemented in the electronics package. The AGC determines the exact attenuation that must be applied to the returned signal to keep constant the output power summed over a fixed number of waveform range gates centered on the track point at frequency f_0 (60 for SEASAT, 48 for GEOSAT, and 32 for TOPEX). The altimeter transmits and receives many pulses per second (1000 for SEASAT and GEOSAT, 4000 for TOPEX). To reduce the geophysical Rayleigh noise in individual received waveforms (Fig. 12), the AGC loop averages all individual waveforms received over $1/20$ s to determine the attenuation value. This AGC value is transmitted to the ground for radar cross-section processing (see Chelton and McCabe 1985) with a $1/16$ dB stepsize for SEASAT and GEOSAT in a 10/s telemetry string. The stepsize will be $1/4$ dB for TOPEX in a 20/s telemetry string. For practical reasons of availability, however, the attenuation is applied onboard the satellite using a digital step attenuator with only 1 dB steps. On the SEASAT altimeter, the same AGC was applied to all 50 pulses in the $1/20$ s average. The power summed over the 60 range gates of the average of 50 waveforms therefore did not in general equal the power desired by the AGC loop. The coarse 1 dB attenuator step size could lead to errors as large as 0.5 dB in the power of the attenuated signal.

Beginning with the GEOSAT altimeter, a new method of applying the AGC was used. The 50 waveforms in each $1/20$ s average were selectively attenuated to achieve very nearly the exact desired AGC value. The method of selective attenuation is most easily described by an example. Suppose the AGC loop determines an attenuation value of 32.7 dB from a group of 50 waveforms. Using the bank of attenuators with 1 dB step sizes, an attenuation of 33 dB is applied to the first 35 waveforms and 32 dB is applied to the last 15 waveforms of the group. The average attenuation over the 50 waveforms is thus the desired 32.7 dB. In this way, an effective AGC resolution of $1/50$ dB is achieved with a 1 dB resolution AGC attenuator. This same method of AGC attenuation will be used on the TOPEX altimeter. Since TOPEX will transmit 4000 pulses per second, the effective AGC resolution in $1/20$ s averages will be $1/200$ dB.

The performance of the AGC is important to the ATU, which attempts to track nadir mean sea level. Recall that the point on the waveform with half the maximum power in the waveform corresponds to nadir mean sea level if the sea surface height distribution is Gaussian. The function of the ATU is to keep this half-power point in the tracking gate (gate 30.5 for SEASAT and GEOSAT, midway between gates 32 and 33 for TOPEX) of the discretely sampled waveform. Shifting the waveform in frequency is equivalent to shifting the range estimate. Frequency shifts are achieved by adjusting the timing of the deramping chirp according to (5) such that the half-power point is maintained in the tracking gate.

Consider the hypothetical waveform in Fig. 11a with flat plateau given by (12) that would be obtained if the antenna gain were 1 across the beamwidth. If the ATU has properly placed the tracking gate at the half-power point of the spectral waveform, then the average power over the group of range gates centered on the tracking gate would be $0.5S_{\max}$ (where $S_{\max}$ is the maximum power in the return waveform). The tracker computes the difference

$$D = S_{\text{agc}} - S_{\text{mid}}, \qquad (16)$$

where S_{mid} is the spectral power in the "middle gate" on the leading edge of the waveform and S_{agc} is the "AGC gate" defined as

$$S_{\text{agc}} = \frac{1}{N_G} \sum_{j=1}^{N_{\text{agc}}} S_j. \qquad (17)$$

In (17), S_j is the spectral power in range gate j, N_{agc} is the number of range gates centered on the tracking frequency f_0 that are included in the AGC gate, and N_G is a normalization factor to make S_{agc} equal to $0.5S_{\max}$. For an idealized antenna with gain of 1 across the beamwidth, N_G is equal to N_{agc}. For SEASAT, N_{agc} was 60 (all of the range gates except the three interleaved gates near the half-power point). To exclude the portion of the waveform most strongly affected by band-edge rolloff from the anti-aliasing filter (see dotted line in Fig. 13), N_{agc} was reduced to 48 for GEOSAT. The TOPEX altimeter will have a much narrower antenna beamwidth than previous altimeters (see section 5b), which will result in greater plateau droop. Consequently, N_{agc} will be reduced even further to 32 range gates centered on the tracking gate.

For proper tracking and noise-free waveforms, S_{mid} is equal to the spectral power in the tracking gate. As noted previously from Figs. 12 and 14, there is residual Rayleigh noise in spectral waveforms, even in averages of a large number of individual waveforms. This noise effectively averages to zero in the $1/20$ s average of the sum over N_{agc} range gates in the waveform. The value of S_{agc} is therefore relatively insensitive to random fluctuations about the mean in each individual range gate. Residual noise can be significant, however, in the average values of S_j over $1/20$ s for any particular range gate j. Thus, setting S_{mid} equal to the spectral value in the tracking gate at frequency f_0 introduces noise in the value of D given by (16).

In practice, noise in the value of S_{mid} is reduced by defining the middle gate as the average of the spectral values at $2k + 1$ frequencies (range gates) centered on the tracking gate frequency f_0. Defining m to be the tracking gate number, the middle gate is given by

$$S_{\text{mid}} = \frac{1}{2k + 1} \sum_{j=m-k}^{m+k} S_j. \qquad (18)$$

The width of the middle gate is adjusted according to the "rise time" of the leading edge of the waveform (directly related to SWH). As wave height increases and the leading edge of the waveform becomes more stretched, the value of k is increased as a staircase function of SWH. A total of five possible middle gate selections are allowed, centered near SWH values of 1, 2, 4, 8, and 16 m. Selection of the appropriate middle gate index k is based on the difference between an "early gate" and a "late gate", each of which consists of averages of several contiguous individual range gates at opposite ends of the leading edge of the waveform. The differences are computed for five different widths of early and late gates, and the pair for which the difference is closest in amplitude to a reference value determines the middle gate index (see Townsend 1980, for more detail). For each SWH gate selection, the width $2k + 1$ of the middle gate is less than the rise time of the mean return, assuring that all of the range gates included in the middle gate are actually on the leading edge of the waveform.

On the SEASAT and GEOSAT altimeters, the middle gate S_{mid} for the two lowest SWH intervals consists of only the tracking gate m (i.e., k is set to zero). Since the TOPEX tracking gate is between range gates 32 and 33, it is not possible to include only one range gate in S_{mid}; the middle gate for the two lowest SWH intervals therefore consists of gates 32 and 33 (i.e., k is set to ½). For all three altimeters, the width of the middle gate doubles for each successively higher SWH interval. The middle gate selection is changed only when SWH changes enough to warrant shifting to a new interval. The ATU is referred to as "adaptive" because of this ability to adjust the width of the middle gate according to SWH.

The value of the AGC gate is only weakly dependent on misalignment of the waveform. The value of the middle gate, however, is very sensitive to waveform alignment. If the difference D given by (16) is greater than zero, then S_{mid} is too small and the half-power point of the leading edge of the waveform was misplaced in a gate earlier than the tracking gate. Similarly, a value of $D < 0$ implies that S_{mid} is too large and the half-power point was misplaced in a gate later than the tracking gate. Assuming that tracking of the half-power point is not off by a large amount (i.e., D is relatively small), then the tracking gate is in the vicinity of the half-power point of the leading edge where the waveform can be approximated as a straight line. Then the shift in frequency necessary to achieve $D = 0$ is

$$\Delta f' = bD, \tag{19a}$$

where b is the reciprocal of the slope of the leading edge at the tracking gate. Since the slope of the leading edge of the waveform is inversely related to SWH, the parameter b is proportional to SWH. This parameter is stored in a look-up table onboard the satellite in the five step sizes corresponding to the middle gate width used in the adaptive tracking.

For a real antenna, the gain pattern results in the plateau droop discussed in section 3 which reduces the average power over the N_{agc} range gates. However, the power in the middle gate remains $0.5S_{\max}$ (for proper tracking), independent of plateau droop. The AGC gate must therefore be adjusted to make D zero for proper tracking by reducing the scaling factor N_G in (17) to account for the plateau droop. The appropriate value for N_G is determined prior to launch from laboratory calibration of the antenna. For SEASAT, N_G was estimated prior to launch to be 53. From postlaunch analysis of SEASAT waveforms, Barrick and Lipa (1981) have suggested that this scaling factor should have been 55. The discrepancy between pre- and postlaunch estimates of the scaling factor was probably due to the use of zero antenna pointing error in the prelaunch simulations. The antenna pointing angle relative to nadir is a nonnegative quantity, and hence has an average value greater than zero. The average pointing angle over the 96-day SEASAT mission was 0.28° (Chelton and McCabe 1985). A nonzero pointing angle increases the spectral power in the plateau region of the waveform (see section 5b and Fig. 15) so that the plateau droop is not as rapid as for zero pointing angle. The correction factor appropriate for zero pointing error would therefore be too small for nonzero pointing angle. Increasing the value of N_G from 53 to 55 can apparently account for the nonzero average pointing angle.

Since the normalization factor N_G necessary to correct for plateau droop varies with antenna pointing angle, no single value of N_G can give an accurate correction for a full range of pointing angles. If a fixed value of N_G is to be used by the ATU, the most logical choice would be to use the value appropriate for the average pointing angle so that, on average, the tracker error due to antenna mispointing is zero. The difficulty is that the average pointing angle is not known prior to launch. Furthermore, deviations about this average pointing angle from pitch and roll of the satellite can be significant. The probability distribution of these deviations depends on the attitude control system used on the spacecraft. Pointing angle deviations from the mean value change the value of S_{agc} and hence D, thus introducing apparent tracking errors even when the ATU has correctly located the half-power point in the tracking gate. These errors are equivalent to using an incorrect value for N_G, but could be corrected in real time by keeping N_G constant and modifying the waveform frequency shift (19a) to have the form

$$\Delta f' = a + bD. \tag{19b}$$

The parameter a accounts for antenna mispointing and depends on the antenna pointing angle, SWH, and the

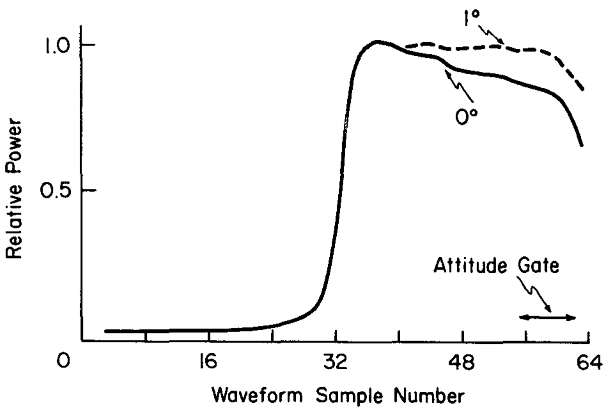

FIG. 15. Example GEOSAT waveforms for 0° (solid line) and 1° (dashed line) off-nadir attitude angle (from MacArthur et al. 1987). The waveform has been normalized to have a maximum value of 1. The attitude gate consisting of the spectral power summed over the last eight waveform samples is shown by the arrow (see section 5b).

antenna gain pattern. It could be stored onboard in a look-up table similar to the parameter b.

The onboard height processing on the SEASAT and GEOSAT altimeters assumed that the parameter a was zero. An attempt is made to remove the error introduced by this assumption in ground-based processing with an "attitude and sea-state correction" in the altimeter sensor file algorithms (Hancock et al. 1980). This ground-based correction also corrects for the SEASAT error in the AGC gate scaling factor N_G discussed above. The formulation (19b) may be preferable to postprocessing. A point of concern, however, is that inclusion of a parameter a in the onboard look-up table requires accurate onboard estimates of antenna pointing angle. This is very difficult (see section 5b). Moreover, there will necessarily be some ground-based corrections to onboard tracking estimates of range anyway, so there may be little advantage to adopting the form (19b) for onboard determination of waveform misalignment.

It should be emphasized that the ATU updates the tracking based on waveforms averaged over $\frac{1}{20}$ s. In the simplest design, the tracker determines the frequency shift required to align the half-power point properly in the tracking gate for one cycle of $\frac{1}{20}$ s waveform averages and then applies this shift to all of the waveforms in the next $\frac{1}{20}$ s cycle. In this way, the ATU updates 20 times per second the frequency shift necessary to locate the track point properly. Frequency shift and time lag between transmitted and deramping chirps are directly related by (5). Thus, the correction Δt_d in timing of the deramping chirp required to shift the waveform by $\Delta f'$ in the frequency domain is

$$\Delta t_d = \frac{\Delta f'}{Q} = \frac{a + bD}{Q}. \qquad (20)$$

In this simple design, the timing of the deramping chirp is shifted by this amount for each pulse in the next $\frac{1}{20}$ s update cycle. The estimate of two-way travel time from the satellite to nadir mean sea level for the next $\frac{1}{20}$ s group of pulses is equal to the adjusted time lag t_d between transmitted and deramping chirps. This travel time measurement is converted to range R_0 from the satellite to nadir mean sea level with the speed of light corrected for independently estimated atmospheric refraction from water vapor, dry gases in the atmosphere (primarily oxygen), and ionospheric free electrons (Chelton 1988). Note that the waveforms in the $\frac{1}{20}$ s average from which waveform misalignment is estimated are not corrected for the frequency shift (19). This is because the waveforms are sampled coarsely by discrete Fourier transforms with frequency resolution of $\delta f = 1/\tau$, as discussed previously. Thus, fine resolution frequency shifts given by (19) are not possible without interpolating the discretely sampled waveform. Since the frequency adjustment is updated 20 times per second, waveform misalignment is generally small, so this is a relatively small source of error in the range measurements.

It is evident from Figs. 12 and 14 that there is some residual noise-like quality of the return signal from Rayleigh fluctuations, even in averages of 1000 waveforms. With the simple tracker design described above, the residual waveform noise in $\frac{1}{20}$ s averages would result in noise in the tracker estimate of the range to nadir mean sea level. Indeed, the largest contribution to Δt_d given by (20) is the noise in the average waveform over $\frac{1}{20}$ s. The estimates of tracking misalignment must therefore be smoothed over time to improve the estimate of frequency shift necessary to align the waveform properly in the sampling gates.

On SEASAT, GEOSAT and TOPEX, smoothing of the estimates of waveform misalignment is implemented with an "α–β tracker," which estimates from (20) the range and range rate of change since the previous tracking update cycle. During each update cycle the ATU estimates the timing of the deramping chirp for the next cycle, $\frac{1}{20}$ s later. The α–β tracker recursion relations for the time lag t_d at which to generate the deramping chirps are

$$\begin{aligned}\dot{t}_d(n) &= \dot{t}_d(n-1) + \beta\Delta t_d(n-1)\\ t_d(n+1) &= t_d(n) + \alpha\Delta t_d(n-1) + \dot{t}_d(n)\\ &= t_d(n) + \dot{t}_d(n-1) + (\alpha+\beta)\Delta t_d(n-1),\end{aligned} \qquad (21)$$

where $\dot{t}_d(n)$ is the timing change from cycle $(n-1)$ to cycle n (the rate of change in timing multiplied by the cycle period), and $\Delta t_d(n-1)$ is the tracking error estimated by (20). The quantities t_d, $\dot{t}_d$ and Δt_d have units of time and α and β are dimensionless. The recursion relations could be expressed equivalently in terms of range and range rate by scaling t_d, $\dot{t}_d$, and Δt_d by the speed of light. During update cycle n, the ATU has previously estimated $t_d(n)$ and $\dot{t}_d(n-1)$ from cycle $(n-1)$. While the pulses for cycle n are transmitted and received, the average waveform from the previous cycle is processed to estimate the tracking error $\Delta t_d(n-1)$ according to (20). Then $\dot{t}_d(n)$ and $t_d(n+1)$ are estimated from the recursion relations. In this way, corrections based on measurements from cycle $(n-1)$ are used to adjust the timing $t_d(n+1)$ of the deramping chirps in cycle $(n+1)$.

If there was no Rayleigh noise in the average waveforms, then the timing errors Δt_d would be noise-free. In this case, the corrected timing for cycle n would be

$$t'_d(n) = t_d(n) + \Delta t_d(n-1), \qquad (22a)$$

where $t_d(n)$ is the timing estimated from cycle $(n-1)$ and $\Delta t_d(n-1)$ is the tracking error determined during cycle n from the average waveform in cycle $(n-1)$. Similarly, the corrected timing change from cycle $(n-1)$ to cycle n would be

$$\dot{t}'_d(n) = \dot{t}_d(n-1) + \Delta t_d(n-1), \qquad (22b)$$

where $\dot{t}_d(n-1)$ is the timing change from cycle $(n-2)$ to cycle $(n-1)$ estimated from the previous cycle. This expression is equivalent to the recursion relation (21) for $\dot{t}_d(n)$ with β set to 1. The ATU estimate of time lag for the deramping chirp for cycle $(n+1)$ would be

$$\begin{aligned} t_d(n+1) &= t'_d(n) + \dot{t}'_d(n-1) \\ &= t_d(n) + \dot{t}_d(n-1) + 2\Delta t_d(n-1). \qquad (22c) \end{aligned}$$

This expression is equivalent to the recursion relation (21) for $t_d(n+1)$ with α and β set to 1. Thus, both α and β would be 1 for noise-free average waveforms in each $1/20$ s update cycle.

To damp out tracking noise due to residual Rayleigh noise in $1/20$ s average waveforms (Fig. 12), the constants α and β must be set to values less than 1. The term $\dot{t}_d$ in the recursion relation (21) is the timing shift of the deramping chirp necessary to account for the vertical component of satellite velocity relative to the sea surface over the $1/20$ s time interval between update cycles. This vertical component of relative velocity is due partly to changes in mean sea level along track and partly to a vertical component of satellite velocity from the small eccentricity of the satellite orbit. The appropriate value of β is chosen based on the maximum range acceleration expected. Based on range acceleration estimates over the Puerto Rico trench, MacArthur (1978) shows that the value of β should be about $1/64$; this is the value used on SEASAT, GEOSAT, and TOPEX. For this value of β, the value of Δt_d would have to be the same for 64 consecutive update cycles for the recursion relations to change $\dot{t}_d$ by the full amount Δt_d. The value of α is chosen to give near-critical damping of the tracker adjustment of waveform misalignment (i.e., to avoid shifting the waveform alignment too much or too little in each tracking update cycle). For a value of $\beta = 1/64$, the appropriate value of α is $1/4$ (MacArthur 1978), which provides a relatively small amount of smoothing of the estimates of time lag between transmitted and deramping chirps.

The vertical component of satellite velocity relative to the sea surface can be as large as 30 m s^{-1}, corresponding to a 1.5 m change in range to mean sea level over the $1/20$ s update cycle. If the shift $\dot{t}_d$, which represents the smoothed change in timing of the deramping chirp over $1/20$ s, was applied to all individual waveforms in the update cycle, the vertical relative velocity would cause the leading edge of the waveform to be artificially stretched in the $1/20$ s average due to the change in 2-way travel time to nadir mean sea level over the $1/20$ s. This would lead to errors in the adaptive tracking estimate of SWH, and hence the range to mean sea level since the constant b in (19) is proportional to SWH. To reduce this effect, the timing shift $\dot{t}_d$ is applied incrementally in steps from zero for the first waveform in the update cycle to the full value $\dot{t}_d$ for the last waveform in the update cycle. For the SEASAT and GEOSAT pulse rates, this corresponds to increments of $\dot{t}_d/50$. The higher TOPEX pulse rate results in increments of $\dot{t}_d/200$. The incrementally applied timing shifts result in a timing change $\dot{t}_d$ per $1/20$ s update cycle that is very nearly correct with little smearing of the average waveform.

It is also possible to include range acceleration (the second derivative of range along track) in an onboard "α–β–γ tracker" algorithm by adding a term $\ddot{t}_d(n)$ to (21), corresponding to the change in timing of the deramping chirp from one update cycle to the next (units of time). However, estimation of acceleration is even more sensitive than velocity to noise in the range measurements and is therefore not accounted for in onboard tracker designs. A correction for range acceleration will be included in the ground processing system for TOPEX. The ground-based correction uses range measurements both before and after update cycle n to estimate acceleration, thus allowing greater smoothing of the noisy range acceleration estimates.

In practice, the actual timing of the deramping chirp can only be changed by relatively coarse steps of 12.5 ns. Finer adjustments are effectively achieved by applying a linear phase rotation to the IF signal in the time domain. If we denote the time series of the IF signal by $\psi(t)$ and its Fourier transform by $\Psi(f)$, it is easy to show that the time series $\psi(t)\exp(i2\pi\Delta f't)$ has Fourier transform $\Psi(f-\Delta f')$. The spectral waveform (13) is computed from

$$S_G(f) = \Psi^*(f)\Psi(f). \qquad (23)$$

A frequency shift of $\Delta f'$ in the return waveform can therefore be achieved by introducing the same frequency shift in $\Psi(f)$. This can be accomplished in the time domain by applying the phase rotation $\phi(t) = 2\pi\Delta f't$ to the IF signal time series $\psi(t)$.

On the SEASAT, GEOSAT, and TOPEX altimeters, the resolution of the phase adjustment is $\phi_{\min} = 2\pi/64$. Since $\phi(t) = 2\pi\Delta f't$, this phase change over the full chirp sweep time τ corresponds to a waveform frequency shift resolution of

$$\Delta f'_{\min} = \frac{\phi_{\min}}{2\pi\tau} = \frac{1}{64\tau}. \qquad (24)$$

From (5), this is equivalent to an effective change in the timing of the deramping chirp by an amount

$$\Delta t_d{}^{\min} = \frac{\Delta f'_{\min}}{Q} = \frac{1}{64\Delta F}. \qquad (25)$$

Since the chirp frequency range ΔF is 320 MHz for all three altimeters, the effective timing resolution of the deramping chirp is 0.0488 ns, which corresponds to a one-way range resolution of about 0.7 cm. The chirp generator allows for a phase angle of $\phi_{\max} = 4\pi$. Applied over the full chirp sweep time τ, this phase change corresponds to a maximum frequency shift of

$$\Delta f'_{\max} = \frac{\phi_{\max}}{2\pi\tau} = \frac{2}{\tau}. \qquad (26)$$

This is equivalent to a change in the timing of the deramping chirp by an amount

$$\Delta t_d{}^{\max} = \frac{\Delta f'_{\max}}{Q} = \frac{2}{\Delta F} = 6.25 \text{ ns}. \qquad (27)$$

Since the phase angle $\phi(t)$ can be added or subtracted, this allows for a timing range of ±6.25 ns, thus completely filling in the range between the coarse 12.5 ns adjustments in the actual timing of the deramping chirp with a resolution of 0.0488 ns.

5. Sources of height tracking errors

The preceding discussion has summarized pulse compression and the tracking method used onboard the satellite to measure the range from the altimeter to mean sea level at satellite nadir. There are a number of instrumental effects which can degrade the tracker performance, thus introducing errors in the range measurement. The largest of these sources of error are described in this section. In some cases the exact magnitudes of these errors are issues of current investigation; only qualitative relative magnitudes are given here for these sources of instrumental error. The intent in this section is to draw attention to the potential sources of greatest concern in instrumental errors.

a. Tracker errors

The most obvious source of tracker errors is noise in the estimates of AGC gate and middle gate values S_{agc} and S_{mid} given by (17) and (18). As described in section 4, S_{agc} is computed from $1/20$ s averages of the sum of a large number N_{agc} of individual range gates in each waveform and is therefore relatively insensitive to Rayleigh fluctuations in the return waveforms. The middle gate S_{mid} is computed from a local average of spectral values around the tracking gate. Because fewer individual range gates are included in the average, S_{mid} is much more sensitive than S_{agc} to Rayleigh noise. This introduces noise in the value D given by (16), which results in errors in the frequency shift $\Delta f'$ in (19) used by the ATU to correct for misalignment of the waveform. For the same amount of noise in D, the error in $\Delta f'$ increases approximately linearly with SWH, since the parameter b in (19) is proportional to SWH. This is mitigated to some degree by the increase in the width of the middle gate (18) with increasing SWH. The noise in D decreases as approximately the square root of the number $2k + 1$ of range gates included in the middle gate. Since the width of the middle gate is approximately proportional to SWH, the noise in D decreases as approximately the square root of SWH. Then the net effect on ATU estimates of waveform misalignment is that the overall noise in $\Delta f'$ increases as approximately the square root of SWH. This unavoidable source of tracker noise is significantly reduced by the time constants α and β used in the recursion relations (21) of the α–β tracker.

A second source of tracker error is systematic errors in S_{agc}. The AGC gate given by (17) must be scaled by N_G to account for plateau droop in the waveforms. If the value of N_G used is not appropriate for the nominal antenna pointing angle (or the prelaunch estimate of nominal pointing angle is incorrect), S_{agc} will be biased. This error could be corrected onboard the satellite by adjusting the parameter a in (19b). As noted previously in section 4, however, the use of the form (19b) for waveform misalignment may not be advantageous since some amount of ground-based postprocessing will be necessary anyway. Any residual systematic errors in the AGC gate would lead to a bias in the estimate of waveform misalignment. As noted in section 4, the prelaunch estimate of N_G for SEASAT was evidently about 4% too small. This error was corrected by ground-based processing.

The look-up table estimate of the parameter b (the reciprocal of the slope of the leading edge of the waveform) in the tracking shift $\Delta f'$ given by (19) introduces a third error in tracker performance. This staircase approximation of the waveform slope is in general not exact, thus introducing errors in waveform alignment. The look-up parameter is based on SWH, with the step size between successive look-up values increasing with SWH. Consequently, this component of tracker noise increases in magnitude with increasing wave height. It might be possible to reduce this source of tracker noise by replacing the table look-up estimate of b with an accurate estimate computed from the actual slope of the leading edge of the waveform. Note, however, that errors in b only affect the rate at which the tracker brings the waveform into proper alignment. A value of b that is too small will require several tracking update cycles to align the waveform properly. A value of b that is too large will result in greater tracker noise as the waveform is shifted too much in each update cycle. Noise introduced by the coarse resolution of b is mitigated, to some extent, by the smoothing inherent in the α–β tracker. These errors are further reduced when the range measurements are averaged over time (1-s averages have been used for most applications of SEASAT and GEOSAT data).

The coarse look-up table resolution of the parameter b in (19) introduces an additional tracking error when the AGC attenuation is in error. For proper tracking, the value of D given by (16) is zero. In this case, D is not sensitive to the accuracy of the AGC attenuation since the same attenuation is applied to the spectral power in all range gates and the tracking gate still coincides with the half-power point. When the value of $D \neq 0$, however, the AGC accuracy becomes more important. Suppose the waveform attenuation is in error by a multiplicative factor C. Then the difference D is also in error by the factor C. The rise-time difference of the leading edge of the waveform is independent of AGC attenuation, so the slope of the leading edge also changes by the factor C. The parameter b therefore changes by the factor $1/C$, and the frequency shift $\Delta f'$ of the waveform given by (19) should be insensitive to the accuracy of AGC attenuation. This is true only if the actual value of the waveform slope is used to compute b. Since b is determined from a coarse look-up table, the error in D is not necessarily compensated for exactly by a similar error in b. Errors in AGC attenuation can therefore introduce noise in the tracking of mean sea level in the waveform. This noise is similar in character to that introduced by errors in b as discussed above. These errors affect the rate at which the tracker brings the waveform into proper alignment.

This AGC attenuation accuracy source of tracker noise was more significant for SEASAT than for GEOSAT and TOPEX because of the different method used to apply attenuation (as discussed in section 4). With SEASAT, the same attenuation was applied to all waveforms in each $\frac{1}{20}$ s update cycle. Since the attenuation could only be applied in 1-dB step sizes, significant attenuation errors (as large as 0.5 dB) were common. This effect is reduced in 1-s averages and in the smoothing applied by the α–β tracker, but may still be an important source of error. With GEOSAT, the AGC loop selectively attenuates the group of 50 waveforms in each $\frac{1}{20}$ s update cycle to achieve $\frac{1}{50}$ dB resolution when averaged over all 50 waveforms. TOPEX will use the same method of selectively attenuating the waveforms in each $\frac{1}{20}$ s update cycle with $\frac{1}{200}$ dB resolution. Residual AGC errors can still result in height tracking errors because of the coarse resolution of the look-up table for the parameter b, but the magnitude of the errors will be much smaller than on SEASAT.

b. Antenna mispointing errors

The combined effects of antenna mispointing and antenna gain pattern can drastically affect the shape of the returned waveform. The total returned power decreases from off-nadir pointing, with the greatest relative decrease near the peak of the return spectral waveform. For large pointing errors, the returned power in the plateau region can actually increase with increasing range gate because the portion of the antenna pattern with maximum gain samples a region on the sea surface away from satellite nadir. An example from the GEOSAT altimeter is shown in Fig. 15. The plateau region of the waveform is horizontal when the satellite attitude angle is equal to the angle corresponding to the half-power point of the antenna gain pattern.

Clearly, antenna mispointing will lead to errors in the AGC gate (17) due to an overestimate of power in the plateau region. Without the shape of the waveform, it would not be possible to distinguish mispointing errors from tracking errors due to a frequency-shifted waveform. As noted in section 4, it might be possible to correct off-nadir antenna pointing errors in real time if the constant a is included in the tracker estimate of waveform misalignment (19b) and accurate onboard estimates of antenna pointing angle are available. Historically, onboard satellite attitude sensors have not provided sufficiently accurate estimates of attitude. Furthermore, the orientation of the altimeter antenna boresight in the satellite coordinate system is known with only limited accuracy. It is probably more practical to correct for errors in the waveform frequency shift estimated by the ATU with ground-based processing.

The antenna pointing angle can be estimated from the shape of the waveform in the plateau region. This method of estimating pointing angle is being used in ground-based postprocessing of GEOSAT data because GEOSAT does not carry an onboard attitude sensor. The method used is to estimate the off nadir angle based on the power summed over the last eight of 60 waveform samples (the "attitude gate"). Empirical corrections based on the attitude estimate are then applied to the estimates of height and SWH (MacArthur et al. 1987). These corrections are functions of both attitude and SWH. From ground simulations, the power in the attitude gate is proportional to the square of the attitude angle. Attitude corrections to altimeter estimates of range and AGC are linearly related to the power of the attitude gate. These corrections are applied using a look-up table formulation with coefficients that depend on SWH.

It is noteworthy that antenna mispointing errors are potentially much more serious for TOPEX than for previous altimeters. The antenna half beamwidth of the SEASAT altimeter was 0.8°. To accommodate the lack of a precise attitude control system (a passive gravity-gradient stabilization system is used instead), the GEOSAT antenna half beamwidth is 1.05°. TOPEX has been designed to have highly precise attitude control and the 13.6-GHz antenna half beamwidth will be only 0.55°. While the narrower beamwidth improves the signal-to-noise ratio in the measurements by focusing the power of the signal incident on the sea surface, the rapid roll-off of the antenna gain pattern causes the AGC gate to be more sensitive to antenna mispointing errors.

c. Waveform sampler calibration errors

Analysis of the average of many spectral waveforms from GEOS-3, SEASAT, and GEOSAT reveals that the power in some range gates is consistently higher or lower by small but significant amounts from that of neighboring range gates. These systematic differences are referred to as waveform (or range-gate) sampler calibration errors. Walsh (1979) discusses these errors extensively for the GEOS-3 altimeter which was distinctly different from later altimeters. GEOS-3 transmitted a swept-frequency pulse similar to SEASAT, GEOSAT, and TOPEX, but with a bandwidth ΔF of 80 MHz rather than 320 MHz. A genuine pulse compression of the received signal was applied using a dispersive delay line. The resulting short duration signal was sampled at 6.25-ns intervals by sample-and-hold circuitry. The range gate sampler calibration errors in GEOS-3 waveforms are evidently due to gain variations in the sample-and-hold circuits. When removed by empirical calibration corrections, the quality of the return waveforms was significantly improved.

Waveform sampler calibration errors should in principle not be present in SEASAT and GEOSAT data since the filter response functions are exactly the same for all range gates with the DFT method of sampling the waveform. Nonetheless, systematic calibration differences do appear to exist between neighboring waveform samples (Hayne 1980; Hayne and Hancock 1987). One cause of these calibration errors is the sharp cutoff anti-aliasing filters implemented on SEASAT and GEOSAT which had significant in-band ripple in the frequency response function. The TOPEX anti-aliasing filter will be designed to have lower in-band ripple, but there will still likely be small variations in the calibration of neighboring range gates. Since the characteristics of the anti-aliasing filters can be determined very accurately by laboratory calibration prior to launch, it should be easy to correct for these in-band ripple effects. Sampler calibrations of this nature can also be determined postlaunch from the average of many noise-only measurements passed through the low-pass anti-aliasing filter.

Another suggested cause for DFT waveform sampler calibration errors is irregularities in the transmitted and deramping chirps. The pulse-compression technique described in section 3 requires an exactly linear frequency change across the chirp sweep period. Known deviations from linear frequency sweep could be accounted for in waveform processing. These could be determined prior to launch from careful laboratory measurements. Variations in the chirp characteristics as the altimeter ages are much more difficult to determine and correct for in waveform processing. They cannot be determined from noise-only measurements. The average of many waveforms from similar sea-state conditions (so that the leading edge of the waveform is the same) must be used. It then becomes difficult to separate sampler gain variations from other geophysical variability that might have similar characteristics. The more exact digital chirp generator used on GEOSAT and TOPEX should greatly reduce this second source of waveform sampler calibration errors.

d. Electromagnetic and skewness bias errors

The function of the ATU as described in section 4 is to maintain the half-power point of the leading edge of the returned waveform in a specific range gate by adjusting the timing of the deramping chirp according to (20). This tracking is performed without regard to the relation between the half-power point and the frequency of the signal returned from mean sea level. There are at least two effects which result in systematic differences between the two. If not corrected for, both of these effects tend to bias the tracker-range estimate below true mean sea level.

The first bias is due to the difference between mean sea level and the mean scattering surface. The radar backscattered power per unit surface area is greater in wave troughs than near wave crests. In part, this is due to the fact that the power backscattered from a wave facet to the altimeter is proportional to the long-wavelength local radius of curvature. Ocean waves are generally skewed such that wave troughs are flat and wave crests are peaked (Fig. 16). Thus, the radii of the troughs are greater than the radii of crests. The result is a bias in backscattered power toward wave troughs. This bias is further enhanced by a greater small-scale roughness of the sea surface near wave crests, which scatters the altimeter pulse in directions away from the incident radiation. A possible physical explanation for the difference in roughness between troughs and crests is that the trough regions are more protected from surface winds, and hence smoother. Troughs are therefore better specular reflectors. Thus, both of these effects bias the power distribution of the reflected altimeter pulse toward wave troughs, as shown in Fig. 17. This bias is due purely to the interaction between electromagnetic (EM) radiation and the sea surface, and is therefore referred to as EM bias. EM bias would probably exist due to the wind effects, even if the sea surface height distribution were Gaussian. This is difficult to

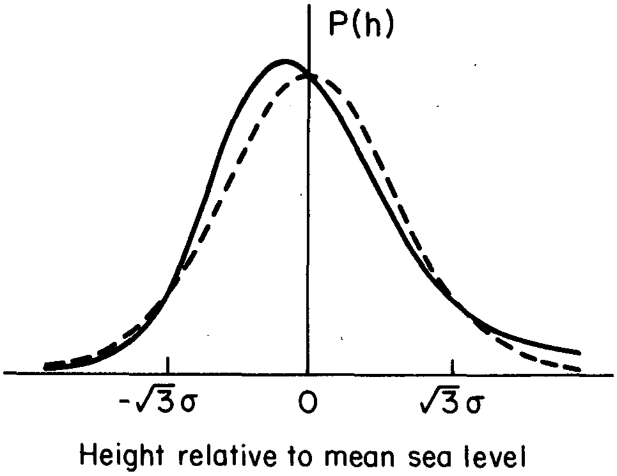

FIG. 16. Comparison of Gaussian (dashed curve) and skewed Gaussian (continuous curve) sea surface height distributions relative to mean sea level. The surface height standard deviation is denoted by σ. Note that the skewed and Gaussian distributions intersect at mean sea level and $\pm\sqrt{3}\sigma$.

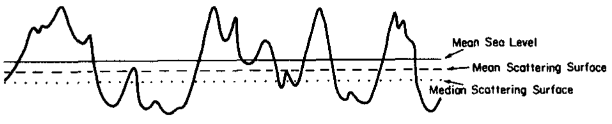

FIG. 17. Schematic representation of mean sea level (thin continuous line), the mean scattering surface (dashed line) and the median of the scattering distribution (dotted line) for a rough sea surface (heavy continuous line).

determine, however, since the sea surface distribution is never exactly Gaussian.

The magnitude of EM bias is difficult to estimate. It cannot be determined from the shape of spectral waveform, since the waveform is shifted in frequency but essentially unchanged in shape (Rodriguez 1988; Walsh et al. 1989), and therefore introduces an undetectable range error. The EM bias probably depends on a variety of surface wave characteristics. The only sea state characteristic measured by the altimeter is SWH (from the slope of the leading edge of the spectral waveform, see section 2). Since EM bias tends to increase with wave height, it is generally expressed as a percentage of SWH. Estimates derived empirically from in-orbit measurements range from 1%–4% of SWH, but with large uncertainty (e.g., Born et al. 1982; Hayne and Hancock 1982; Douglas and Agreen 1983).

The magnitude of the EM bias can be quite large. Significant wave heights of 10 m are not uncommon in the Southern Ocean (Chelton et al. 1981). If the EM bias is 2% of SWH, this corresponds to a bias of 20 cm. If the uncertainty of the EM bias is only 1% of SWH, the resulting uncertainty in the range measurements is 10 cm. This clearly represents a major source of uncertainty in the overall height error budget.

The second bias is related to the non-Gaussian nature of the sea surface height distribution. Removing the EM bias discussed above, the correspondence between the half-power track point and mean sea level is exact only if the distribution of specular scatterers is Gaussian. In actual fact, the height distribution (and hence the distribution of specular scatterers) is skewed (Fig. 16). Mean sea level is unchanged. However, the amplitudes of negative height deviations are reduced, and the amplitudes of positive height deviations are increased by skewness in the height distribution. The median of the height probability density function $p(h)$ corresponds to the point $h_{\rm med}$ where

$$\int_{-\infty}^{h_{\rm med}} p(h)dh = \int_{h_{\rm med}}^{\infty} p(h)dh = 0.5. \qquad (28)$$

For any symmetric distribution such as a Gaussian, the median is equal to the mean value. The median of a skewed Gaussian sea surface height distribution is shifted from mean sea level toward the wave troughs (Hayne and Hancock 1982; Srokosz 1986). Since the spectral waveform (13) is an integral of the probability density of specular scatterers (weighted by the antenna gain), the half-power point on the leading edge corresponds very closely to the median of the scattering surface. Effects such as antenna pointing errors and the roll-off of the antenna gain pattern will cause the half-power point to differ from the median, but these differences are second-order effects. This tracker height bias toward wave troughs due to the non-Gaussian nature of the sea surface height distribution is referred to as the "skewness bias" (Fig. 17).

At the present time, estimates of the magnitude of the skewness bias are very uncertain, ranging from 20%–100% that of the EM bias (though not in any simple way related to EM bias). Correcting for the skewness bias requires knowledge of both the surface wave height standard deviation (or, equivalently, SWH) and the skewness parameter. Determination of the latter is possible from ground-based analysis of waveforms (Rodriguez 1988; Walsh et al. 1989), but requires very accurate range-gate calibrations (see section 5c). Rodriguez (1988) and Rodriguez and Chapman (1988) have estimated skewness biases of 1–4 cm from simulations and actual SEASAT data.

Clearly, further research is important to understanding better the physical basis of the EM and skewness biases and developing accurate correction algorithms.

e. Doppler shift errors

As noted in section 4, the vertical component of satellite velocity relative to the sea surface can be as large as 30 m/s. Velocities of this magnitude introduce a Doppler shift in the frequency of the return signal received by the altimeter. Since the frequency of the IF signal produced by pulse compression is directly related to the range to mean sea level, a Doppler shift in frequency introduces an error in the altimeter range estimate.

The two-way Doppler shift for a transmitted frequency F is given by

$$\Delta f_D = \frac{2v}{c} F, \qquad (29)$$

where v is the vertical component of relative velocity and c is the speed of light. From (7), the two-way travel time delay due to Doppler shift is

$$\Delta t_D = \frac{\Delta f_D}{Q}. \qquad (30)$$

The corresponding height error is

$$\Delta h_D = \frac{c\Delta t_D}{2} = \frac{vF}{Q}. \qquad (31)$$

For the SEASAT chirp center frequency of $F_0 = 13.5$ GHz and chirp frequency range $\Delta F = 320$ MHz, the Doppler frequency shift varied by only 2.35% across the chirp. This variation is negligible and the Doppler frequency shift can be considered constant across the chirp. With the SEASAT chirp frequency sweep rate of Q = 100 kHz/ns, the Doppler shift range error for a vertical velocity of 30 ms^{-1} is approximately 0.4 cm. Range errors of this magnitude were negligible in the overall height error budget for the SEASAT altimeter. Consequently, Doppler effects were ignored in SEASAT data processing.

The longer chirp period (lower sweep rate) of the GEOSAT altimeter results in larger timing errors from Doppler effects. The GEOSAT sweep rate of Q = 3.125 kHz/ns corresponds to a Doppler shift range error of 13.0 cm for a vertical relative velocity of 30 m/s. Errors of this magnitude are significant in the GEOSAT total height error budget. The Doppler shift error is similar in nature to the EM bias in that the return waveform is shifted in frequency but otherwise unchanged in shape and therefore introduces an undetectable range error. It also cannot be determined from the waveform itself, so it must be estimated independently. For GEOSAT, the Doppler correction is applied in the ground processing system based on estimates of the vertical component of satellite velocity from the α–β tracker.

The dual frequency TOPEX altimeter incorporates two center frequencies of 13.6 and 5.3 GHz, both with 320 MHz chirp frequency range. The pulse durations and frequency sweep rates will be the same for both frequencies as that used on GEOSAT. A 30 m s^{-1} vertical component of velocity results in a Doppler shift range error of approximately 13.1 cm for the 13.6 GHz frequency. For the lower 5.3 GHz TOPEX frequency, the Doppler shift range error is proportionally smaller according to (31), though still not negligible. Ignoring the 6% Doppler dispersion across the 320 MHz frequency range of the 5.3 GHz chirp, a vertical relative velocity of 30 ms^{-1} results in a range error of 5.1 cm. The Doppler shift errors at both TOPEX frequencies will be corrected in the ground data processing system as with the GEOSAT data.

f. Cloud and rain attenuation

Clear atmosphere is relatively transparent to the microwave frequencies of interest to satellite altimetry. There is some attenuation (rarely exceeding a few percent—see Maul 1985; Stewart 1985) by water vapor in the atmosphere. However, even large attenuation by water vapor has little effect on altimeter tracker performance. This is because the spatial scales of water vapor are large (order 100 km or larger) so that water vapor would attenuate the return power by very nearly the same amount over the altimeter footprint. Consequently, the returned power in all of the frequency range gates would be attenuated by approximately the same amount. This is compensated for by the AGC so that the shape of the waveform analyzed by the ATU is relatively insensitive to large spatial scale attenuation. (Note that the refractive effects of water vapor on microwave radiation cannot be ignored in determining the range from the satellite to the sea surface from the measured two-way travel time—see Chelton 1988. These refractive effects have negligible effect on the shape of the return waveform, however, and therefore do not affect tracker performance.)

The presence of clouds or rain in the altimeter footprint can affect tracker performance. At microwave frequencies, attenuation by clouds and rain increase with increasing frequency of the transmitted signal (Maul 1985; Stewart 1985). For the 5.3 GHz TOPEX altimeter, cloud and rain attenuation are both very small. Attenuation can be large, however, for the 13.5 GHz SEASAT and GEOSAT altimeters and the 13.6 GHz TOPEX altimeter. As with water vapor in the atmosphere, homogeneous clouds or rain cells across the altimeter footprint have only a minor effect on tracker performance since the return power is attenuated by approximately the same amount in all of the frequency range gates. Spatial inhomogeneities in the distribution of clouds or rain can introduce significant tracking errors. Small scale clouds or rain cells attenuate only selected range gates. This results in errors in the AGC gate S_{agc} and middle gate S_{mid}, given by (17) and (18), which leads to errors in the frequency shift $\Delta f'$ in (19) used by the ATU to correct for misalignment of the waveform. Since S_{mid} consists of an average over a smaller number of range gates, it is more sensitive than S_{agc} to attenuation errors from cloud or rain effects. Thus, inhomogeneities in clouds or rain cells near satellite nadir, corresponding to the portion of the return waveform near the leading edge, introduce the largest tracking errors.

Attenuation by clouds depends on the cloud temperature (i.e., the cloud altitude), thickness, and density (Fig. 18a). The greatest attenuation is for dense, high clouds. At 13.6 GHz, the two-way attenuation for a dense 2 gm m^{-3}, low cloud with temperature 273°K is about 0.3 dB/km. This increases to 0.9 dB/km for a dense, high cloud with temperature 265°K. Attenuation by isolated small-scale clouds is relatively minor. The largest tracking errors are caused by parallel cloud streets oriented orthogonal to the satellite ground track. Walsh et al. (1984) have shown that the magnitude of the deviations increases with the cloud street spacing, oscillating between ±2.6 cm for a 5 km along-track spacing. Since the horizontal spacing of cloud streets is on the order of the height of the boundary layer (rarely exceeding twice the height of the boundary layer), 5 km is a reasonable upper bound on the spacing of cloud streets. The ground speed of altimetric satellites is 6–7 km s^{-1}. Thus, the oscillating errors introduced by attenuation of the transmitted signal from cloud streets are reduced to small values when the altimeter range measurements are averaged over periods of 1 s or longer.

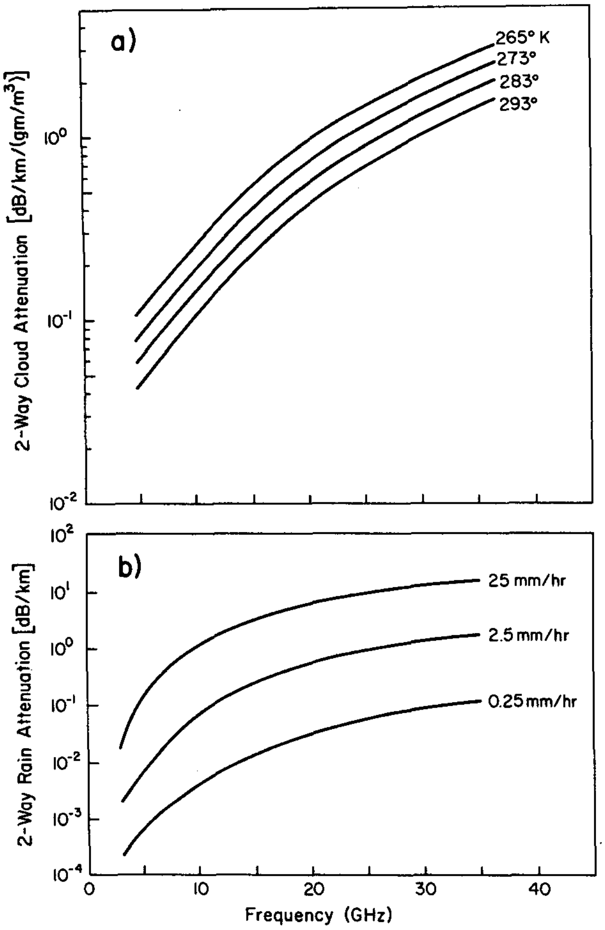

FIG. 18. Two-way attenuation as a function of microwave frequency of the altimeter pulse for (a) clouds, and (b) rain. The rain attenuation is for a temperature of 291°K. Curves were generated from one-way attenuation data given by Maul (1985).

The effects of rain attenuation on tracker performance can be much more significant, depending on the spatial scale of the rain cells and on the rain rate. Attenuation by rain increases with rain rate (Fig. 18b). At 13.6 GHz, the two-way attenuation increases from about 0.2 dB/km for a rain rate of 2.5 mm h^{-1}, to 2.4 dB/km for a rain rate of 25 mm h^{-1}. The cumulative probability distribution of rain measured over land (Goldhirsch 1983) indicates that rain rates exceed 2 mm h^{-1} about 1% of the time, and exceed 10 mm h^{-1} only about 0.2% of the time. The statistics of rain rates over the ocean are not well known. Ocean areas do not have the localized ground heating that generates most of the convective cells over land, so typical rain rates over the ocean are likely smaller than over land. This is supported by observations in extreme rain conditions associated with a hurricane. Marks (1985) measured rain rates in Hurricane Allen, which had a precipitation distribution similar to that of a tropical squall line. The average rain rate in the eyewall of the hurricane was 11.3 mm h^{-1}. In the rainband regions surrounding the eye, the average rain rate was only 1.8 mm h^{-1}. Rain rates exceeding 25 mm h^{-1} covered only 1% of the total area within a 111-km radius of the center of the hurricane, and 95% of the area covered by these high rain rates occurred in the eyewall region.

Monaldo et al. (1986) computed tracker errors for a realistic horizontal profile of attenuation from rain rates estimated by ground-based radar measurements of a rain storm over land with maximum rain rate of 25 mm h^{-1}. Horizontal inhomogeneities in rain rates resulted in tracker errors that oscillated between extremes of −15 cm and +25 cm over along-track distances of 5–10 km. An example of apparent rain contamination of GEOSAT height measurements is given in Cheney et al. (1987). These large tracking errors may still be significant in 1-s averages of altimetric range measurements. Data contaminated by rain attenuation can usually be detected as a high standard deviation of the individual range measurements included in the average, or by anomalous values of SWH. With the TOPEX altimeter, it will also be possible to flag altimeter measurements in regions of high rain rates estimated from passive microwave measurements of brightness temperatures at 18, 21, and 37 GHz.

6. Summary

Satellite altimetry is relatively unique among spaceborne oceanographic remote sensing techniques in that it has spanned more than one and a half decades of experience. There has been an orderly transition from one generation of altimeters to the next, with significant improvements in measurement precision and accuracy with each new altimeter. Since the earliest satellite altimeter on SKYLAB in 1973, the emphasis has shifted from proof of concept, where oceanographic signals even as large as the Gulf Stream were ambiguous in the data, to a point where tracking of individual features such as eddies with only a few cm amplitude is possible. To achieve this level of accuracy, more than a dozen corrections must be applied for instrumental errors, atmospheric refraction, and external geophysical effects. Each of these corrections must be accurate to better than a few cm to achieve an overall accuracy of 5–10 cm. This pushes the limits of present capabilities.

The physical basis for each of the atmospheric and external geophysical corrections is well understood. The instrumental effects are less well understood. In this paper, we have summarized the instrumental technique used onboard the satellite to extract an estimate of mean sea level from the signal transmitted and received by the altimeter. A pulse-compression technique is used to obtain the same information from a relatively long transmitted pulse that would be obtained by transmitting a very short pulse and measuring the time history of the return in a sequence of range gates. The long pulse consists of a chirp with linear frequency change over the pulse duration. The signal returned from the sea surface is then differenced with a deramping chirp that is identical to the transmitted chirp except that the frequency is lower by an "intermediate frequency" difference of $f_{\rm IF}$. The power spectrum of this IF signal, referred to as the return waveform, is analogous to the time series of returned power that would be obtained from a very short pulse. The only difference is that the independent variable for the spectral waveform (the abscissa in a plot of the waveform) is frequency rather than time. There is a direct correspondence between frequency in the waveform and two-way travel time for the pulse to propagate from the altimeter to the sea surface and back. Thus, pulse compression is effectively equivalent to transmitting and receiving an actual short pulse.

Given the probability distribution of the sea surface elevation, the pulse reflected from nadir mean sea level can be associated with a particular point on the return waveform. For a Gaussian sea surface height distribution, this corresponds to the half-power point on the leading edge of the waveform. The altimeter onboard tracker shifts the waveform in frequency to maintain the half-power point in a particular range gate. This shift is achieved by adjusting the timing of the deramping chirp. For proper tracking, the time lag between the transmitted and deramping chirps is equal to the two-way travel time from the altimeter to mean sea level at satellite nadir. The speed of light used to transform from two-way travel time to range must account for the effects of atmospheric refraction from water vapor and dry gases in the troposphere, and ionospheric free electrons. These corrections and their accuracies are discussed in Chelton (1988).

The precision and accuracy of the sea surface height measurement obtained by pulse compression and adaptive tracking of the half-power point are dependent on a number of factors. The major sources of instrumental error are discussed in section 5. Height errors introduced by automatic gain control and waveform sampler calibration errors can be controlled by careful instrument design and prelaunch calibration experiments. The amplitudes and along-track time scales of these errors (i.e., wavelengths of the height errors introduced by these effects) need to be investigated. Antenna mispointing errors can be corrected if accurate estimates of antenna pointing angle are available. The accuracy of pointing angle estimates obtained from the power in the trailing edge of the return waveform needs to be quantified. Doppler shifts in the frequencies of the returned signals introduce a height bias that can be easily corrected in ground data processing based on the vertical component of satellite velocity relative to the sea surface estimated by the α–β tracker. The effects of cloud attenuation of the transmitted signal on the accuracy of altimeter range measurements are relatively small in the 1-s averages generally used in geophysical applications. Rain attenuation can be significant, however, and is best dealt with by excluding from analysis all data flagged as contaminated by rainfall.

The least understood components of height error are the EM and skewness biases that result from an uneven distribution of short-scale surface roughness on the wave field (greater roughness near wave crests) and the inherently non-Gaussian nature of the sea surface height distribution. The physical basis for these two effects is understood qualitatively, but not well enough in detail to make accurate corrections to the height measurements. At present, the uncertainty in these bias corrections is as large as the corrections. Further theoretical and experimental work is required to understand better the nature of these two effects and to develop the most appropriate correction algorithms.

Acknowledgments. We would like to acknowledge many helpful discussions with George Hayne, Lee-Lueng Fu, David Hancock and Ray Stanley, and comments by Philip Callahan and George Born on an earlier draft of the manuscript. We also thank George Hayne, Lee-Lueng Fu and an anonymous reviewer for detailed, constructive reviews of the final manuscript. The work described in this paper was carried out while one of the authors (DBC) was a visiting scientist at the National Center for Atmospheric Research (NCAR). We gratefully acknowledge the use of NCAR facilities and support from the Oceanic Processes Branch of NASA and Contract 958127 from the Jet Propulsion Laboratory funded under the TOPEX Announcement of Opportunity.

APPENDIX A

Altimetry on a Spherical Earth

Since the antenna beamwidths used in satellite altimetry are small (typically 1°–2°), it would seem that the surface of the earth in the altimeter footprint could be closely approximated by a plane locally tangential to the nadir point. This flat earth approximation was used in SEASAT and GEOSAT processing to determine the altimeter footprint area and normalized radar cross section. The spherical-earth solutions to these quantities are derived in this appendix and it is shown that neglecting the curvature of the earth results in non-negligible errors of more than 10%. For the higher TOPEX orbit altitude, the errors increase to about 20%, making it even more important that the spherical earth solutions be used in the TOPEX processing.

Also included in this appendix is a derivation of the antenna gain pattern expressed as a function of the frequency of the signal returned from the sea surface on a spherical earth. This form of the gain pattern is used in the convolution expression (13) for the shape of the return spectral waveform in section 3.

A1. Altimeter footprint area

The geometry of a satellite orbiting the earth at an altitude R_0 above the sea surface is shown in Fig. 19.

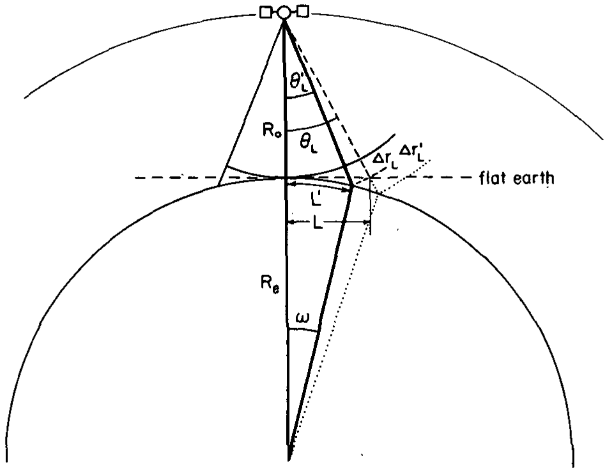

FIG. 19. Geometry of an altimeter footprint from an altitude R_0 above the sea surface at satellite nadir for a flat earth (horizontal dashed line) and spherical earth of radius R_e. For a fixed one-way incremental slant range Δr_L relative to R_0, the off-nadir angles for a flat (dashed line) and spherical (solid line) earth are θ_L and θ'_L, respectively. The corresponding distances along the sea surface are L and L'. The angle measured from the center of the earth for the arc from satellite nadir to the point a distance L' along the curved earth surface is ω. Also shown in the figure by dotted lines is the incremental slant range $\Delta r'_L$ for antenna angle θ_L and a spherical earth.

Consider an off-nadir angle θ_L. Define the slant range from the satellite to a flat earth along angle θ_L to be

$$R_L = R_0 + \Delta r_L, \qquad (32)$$

where Δr_L is the incremental slant range compared with the nadir altitude R_0 (see Fig. 19). For speed of light c, this incremental slant range is associated with a particular two-way travel time Δt_L relative to the time that the pulse reflected from satellite nadir is received by the antenna,

$$\Delta r_L = c\Delta t_L/2. \qquad (33)$$

The angle θ_L intersects the sea surface on a flat earth a distance L from satellite nadir.

Now consider the same relative two-way travel time Δt_L and associated incremental slant range Δr_L on a spherical earth. Because of the curvature of the earth, the off-nadir angle for a given two-way travel time is smaller than the value θ_L for the flat-earth approximation. The off-nadir angle for a spherical earth is shown as θ'_L in Fig. 19, which intersects the sea surface a distance L' from satellite nadir along the spherical earth surface. The arc length L' can be determined from the radius of the earth R_e and the angle ω measured from the center of the earth. Define the radius of the satellite orbit to be

$$H = R_0 + R_e. \qquad (34)$$

The angle ω can be determined from the lengths H, R_L, and R_e of the three sides of the triangle shown by the heavy lines in Fig. 19. Let

$$s = \frac{1}{2}(H + R_L + R_e). \qquad (35)$$

The angle ω is related to s by the trigonometric identity

$$\sin\omega = \frac{2}{HR_e}[s(s - R_L)(s - H)(s - R_e)]^{1/2}. \qquad (36)$$

Since altimeter antenna half-beamwidths are small (typically less than about 1°), the angle ω is small and $\sin\omega \approx \omega$. Then substituting for R_L and H from (32) and (34),

$$\omega \approx \sin\omega = \frac{1}{R_e}\left[\frac{2R_0\Delta r_L}{1 + R_0/R_e}\right]^{1/2}. \qquad (37)$$

The arc length L' along the spherical earth surface is

$$L' = R_e\omega = \left[\frac{2R_0\Delta r_L}{1 + R_0/R_e}\right]^{1/2} = \left[\frac{R_0 c\Delta t_L}{1 + R_0/R_e}\right]^{1/2}. \qquad (38)$$

The flat-earth approximation L corresponds to $R_e = \infty$. The distance L' on a spherical earth is therefore related to the flat-earth approximation L by

$$L' = \frac{L}{(1 + R_0/R_e)^{1/2}}. \qquad (39)$$

It is apparent that the curvature of the earth reduces the altimeter footprint radius for fixed two-way travel time Δt_L. The radius of the earth is approximately $R_e \approx 6371$ km. For the SEASAT and GEOSAT altitudes of 800 km, this results in a 5.8% reduction in footprint radius. The reduction is 9.1% for the higher TOPEX altitude of 1335 km. The footprint diameters on a spherical earth are given for various values of SWH in Table 1 in section 2.

The altimeter footprint area for a given two-way travel time Δt_L is

$$\begin{aligned} A' &= \pi L'^2 \\ &= \frac{\pi R_0 c\Delta t_L}{1 + R_0/R_e} \\ &= \frac{A}{1 + R_0/R_e}, \end{aligned} \qquad (40)$$

where A is the flat-earth approximation to the footprint area, corresponding to $R_e = \infty$. The curvature of the earth thus reduces the footprint area for fixed two-way travel time by 11.2% for SEASAT and GEOSAT, and 17.3% for TOPEX.

A2. Normalized radar cross section

The change in footprint area for a spherical earth has important repercussions for determination of normalized radar cross section from altimeter radar returns. The return power received by the altimeter antenna is related to the transmitted power P_T by the radar equation (Skolnik 1970; Stewart 1985),

$$P_r = T^2 \frac{P_T G^2 c^2}{(4\pi)^3 R_0{}^4 F_0{}^2} \sigma, \qquad (41)$$

where G is the boresight antenna gain, F_0 is the center frequency of the transmitted and received signal, σ is the scattering cross section of the sea surface, and T is the transmittance of the atmosphere (ranging from 1 for a transparent atmosphere to 0 for an opaque atmosphere). For the microwave frequencies of interest to altimetry, t is very nearly equal to 1, except in the presence of dense, thick clouds or rainfall (see section 5f).

The scattering cross section σ has units of area and is determined by the surface roughness, which is related to winds near the sea surface (Chelton and McCabe 1985; Chelton and Wentz 1986). Physically, σ can be thought of as the cross-sectional area of an equivalent point target in the altimeter footprint. For distributed targets such as the sea surface, the scattering characteristics are described by the normalized radar cross section σ_0, which is defined to be the scattering cross section per unit area and is related to σ by

$$\sigma = \int_A \sigma_0 dA, \qquad (42)$$

where A is the illuminated area on the sea surface (which differs from the total oceanographic footprint area contributing to the radar return, see section 2). Note that σ_0 is independent of the altimeter pulse-limited footprint and is thus a measure only of the scattering characteristics of the sea surface, regardless of the antenna characteristics. If σ_0 is uniform over the footprint area, then the radar equation (41) can be expressed in the alternative form

$$\sigma_0 = \frac{\sigma}{A} = \frac{(4\pi)^3 R_0{}^4 F_0{}^2}{T^2 G^2 c^2 A} \frac{P_r}{P_T}. \qquad (43)$$

The area used to determine σ_0 by (43) is the sea surface area reflecting the radar pulse within the expanding annulus of the pulse-limited footprint. This illuminated area is shown in section 2 to be the area (2a) on a spherical earth corresponding to an incremental two-way travel time $\Delta t = \tau$, where τ is the effective pulse duration (after pulse compression), equal to 3.125 ns for SEASAT, GEOSAT, and TOPEX.

For the SEASAT and GEOSAT altimeters, the flat-earth approximation of the area illuminated by the radar was used in the determination of σ_0. As noted previously from (40), the area on a spherical earth is smaller than the flat-earth approximation by the factor $(1 + R_0/R_e)^{-1}$, which is equal to 0.888 for the SEASAT and GEOSAT altitudes of 800 km. If the calculated normalized radar cross sections for a spherical-earth and flat-earth approximation are denoted by σ_0' and σ_0, respectively, then from (40) and (43),

$$\sigma_0' = \frac{A}{A'} \sigma_0 = (1 + R_0/R_e)\sigma_0. \qquad (44a)$$

For SEASAT and GEOSAT, the normalized radar cross section for a spherical earth is thus 12.6% higher than the flat-earth approximation. For the higher TOPEX orbit, the spherical-earth solution is 20.9% higher than the flat-earth approximation.

The error of the flat-earth approximation explains part of the discrepancy between measurements of normalized radar cross section by the SEASAT altimeter and 0° incidence-angle scatterometer noted by Chelton and Wentz (1986) and reproduced here as Fig. 20. Expressed in terms of dB, the relation (44a) between spherical-earth and flat-earth solutions for normalized radar cross section becomes

$$\sigma_0' \,(\text{dB}) = \sigma_0 \,(\text{dB}) + 10 \log_{10}(1 + R_0/R_e). \qquad (44b)$$

For the SEASAT altitude of 800 km, the spherical earth correction to σ_0 given by the second term in (44b) shows that the flat-earth approximation is 0.51 dB. This is in remarkable agreement with the bias between altimeter and scatterometer σ_0 over the range from about 10 dB to 16 dB (which encompasses 78% of all SEASAT observations of σ_0) evident from Fig. 20. Note that a flat-earth approximation at the higher TOPEX altitude of 1335 km introduces a bias of −0.83 dB.

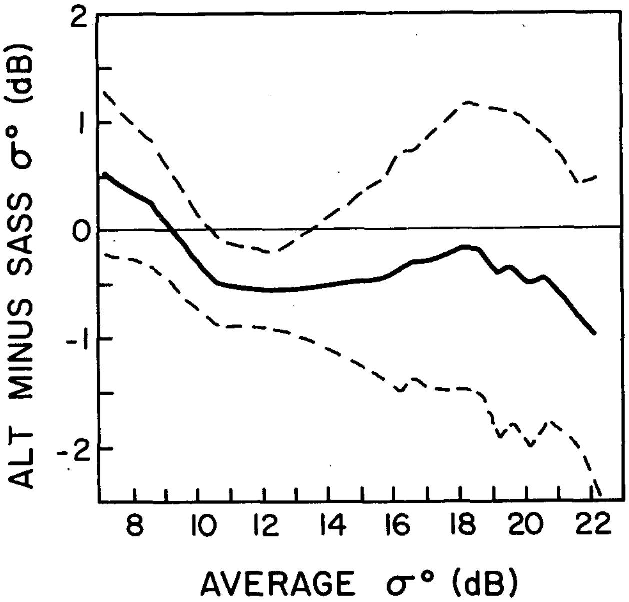

FIG. 20. Comparison of altimeter (ALT) measurements of σ_0 and SEASAT scatterometer (SASS) measurements of σ_0 at 0° incidence angle (from Chelton and Wentz 1986). For both datasets, σ_0 was averaged over 50 km in the along-track direction. Continuous line represents average difference (ALT minus SASS) for σ_0 bin sizes of 0.5 dB and dashed lines correspond to the one-standard deviation scatter about the average difference in each bin. Note that the statistical reliability of the comparison is low for $\sigma_0 > 16$ dB because of the small number of σ_0 observations in this range.

It thus appears that the error in the flat-earth approximation used to compute σ_0 for the SEASAT altimeter can account for much of the observed discrepancy between altimeter and scatterometer measurements of σ_0. Note that the flat-earth approximation cannot explain the linearly increasing bias between altimeter and scatterometer measurements for values of σ_0 less than 10 dB. These small values of σ_0 correspond to high wind speeds (and hence, high sea states). This linearly increasing error may in part be due to sea-state bias errors not accounted for in the calculation of σ_0, as suggested by Chelton and Wentz (1986).

A3. Antenna gain pattern

The spherical-earth corrections to flat-earth approximations summarized in this appendix can also be used to determine the antenna gain pattern $G(\theta_L)$ expressed in section 3 as a function of frequency of the returned signal. This form of the gain pattern is required for the convolution expression (13) for the return spectral waveform shown in Fig. 11b. In section A1 the relationship between flat-earth and spherical-earth off-nadir angles for a fixed incremental slant range was derived. In this section, we derive the relationship between flat-earth and spherical-earth incremental slant ranges for a fixed off-nadir angle. For off-nadir angle θ_L, the actual incremental range to the sea surface on a spherical earth is $\Delta r'_L$, as shown by the dotted lines in Fig. 19. Define the total slant range from the satellite to the spherical earth surface to be

$$R'_L = R_0 + \Delta r'_L. \qquad (45)$$

Then, letting

$$s' = \frac{1}{2}(H + R'_L + R_e), \qquad (46)$$

the angle θ_L is related to s' by the same trigonometric identity used earlier,

$$\theta_L \approx \sin\theta_L = \frac{2}{HR'_L}[s'(s' - R'_L)(s' - H)(s' - R_e)]^{1/2}. \qquad (47)$$

The approximation is for the small off-nadir angles relevant to satellite altimetry. Substituting for H and R'_L from (34) and (45),

$$\theta_L \approx \left[\frac{2\Delta r'_L}{R_0(1 + R_0/R_e)}\right]^{1/2}. \qquad (48)$$

Then the incremental slant range to the spherical-earth surface is

$$\Delta r'_L = \frac{R_0\theta_L{}^2}{2}(1 + R_0/R_e). \qquad (49)$$

The term in parentheses is the spherical-earth correction to the flat-earth approximation Δr_L in Fig. 19. This correction factor increases the incremental slant range by 10%–20%, depending on the satellite altitude R_0.

From (33), the two-way travel time associated with the incremental slant range $\Delta r'_L$ is

$$\Delta t'_L = \frac{2\Delta r'_L}{c} = \frac{R_0\theta_L{}^2}{c}(1 + R_0/R_e). \qquad (50)$$

The frequency of the IF signal corresponding to this two-way travel time is given by (11) in section 3,

$$\begin{aligned} f_L &= f_0 + Q\Delta t'_L \\ &= f_0 + \frac{QR_0\theta_L{}^2}{c}(1 + R_0/R_e), \end{aligned} \qquad (51)$$

where $Q = \Delta F/\tau$ is the frequency sweep rate of the transmitted chirp with frequency range ΔF and duration τ. This frequency is used in (14) to express a Gaussian antenna gain pattern $G(\theta_L) = \exp[-g\theta_L{}^2]$ (where g is the Gaussian decay rate) as a function of frequency,

$$G(f) = \exp\left[-\frac{cg(f_L - f_0)}{QR_0(1 + R_0/R_e)}\right]. \qquad (52)$$

This is the form of the antenna gain pattern used in section 3 in the convolution expression (13) for the frequency description of the return spectral waveform.

APPENDIX B

Glossary of Symbols

a	Offset factor used to account for antenna pointing errors in the frequency shift of the waveform given by (19b).
A	Flat-earth approximation to the altimeter pulse-limited footprint area (appendix A).
A'	Pulse-limited footprint area on a spherical earth (appendix A).
A_{ann}	Pulse-limited area of the sea surface footprint annulus given by (4) on a spherical earth.
$A_{\text{in}}(t)$	Pulse-limited area within the inner circle of the sea surface footprint annulus (defined by the trailing edge of the pulse) given by (3) on a spherical earth.
A_{max}	Pulse-limited maximum area of the circular sea surface footprint with expanding outer diameter as the footprint just becomes an annulus as given by (2) for a spherical earth.
$A_{\text{out}}(t)$	Pulse-limited area within the outer circle of the sea surface footprint (defined by the leading edge of the pulse) given by (1) for a spherical earth.
α	Time constant used in the α–β tracker recursion relations (21) to set the timing

	of the deramping chirps in the next $^1/_{20}$ s update cycle.
AGC	Automatic Gain Control used to reduce the spectral power in a fixed number of range gates centered on the tracking frequency f_0 so that the total power summed over these range gates is normalized to a constant value.
ATU	Adaptive tracking unit used to shift the return waveform in the frequency domain by adjusting the timing of the deramping chirp.
b	Multiplicative factor used to account for the slope of the leading edge of the waveform in the shift of the waveform in the frequency domain given by (19a) and (19b).
β	Time constant used in the α–β tracker recursion relations (21) to account for the vertical velocity of the satellite relative to the sea surface.
c	The speed of light (2.998×10^8 m/s in free space).
C	Multiplicative factor of AGC attenuation error in section 5a.
D	The difference between spectral power in the AGC gate and the middle gate, as given by (16).
DFT	Discrete Fourier transform.
f	Frequency in the return spectral waveform of the IF signal.
F	Frequency in the transmitted chirp.
f_C	Frequency of the IF signal corresponding to the return from a wave crest as given by (6) in the idealized case of only three reflecting points on the sea surface (Figs. 7 and 8).
f_{IF}	Center frequency of the IF signal obtained by differencing the signal returned from the sea surface with a deramping chirp generated internally by the altimeter.
f_0	Frequency of the IF signal corresponding to the return from mean sea level at satellite nadir as given by (6).
f_L	Frequency of the IF signal corresponding to the return from mean sea level a distance L from satellite nadir as given by (11).
$f_{\max}$	Maximum frequency included in the return waveform after low-pass filtering with an anti-aliasing filter (Fig. 13).
$f_{\min}$	Minimum frequency retained in the return waveform (Fig. 13).
f_N	Nyquist frequency for a discretely sampled time series. For a sample interval of δt, the Nyquist frequency is $f_N = 1/(2\delta t)$.
f_T	Frequency of the IF signal corresponding to the return from a wave trough as given by (6) in the idealized case of only three reflecting points on the sea surface (Figs. 7 and 8).
F_0	Center frequency of the altimeter transmitted chirp.
δf	Frequency resolution (i.e., frequency interval between independent samples) for the IF time series. For a record length τ, the frequency resolution is $\delta f = 1/\tau$.
Δf	Frequency difference in the return spectral waveform relative to the frequency f_0 of the signal received from mean sea level at satellite nadir, as given by (7).
ΔF	The total frequency range in the altimeter transmitted chirp centered on frequency F_0.
Δf_D	Two-way Doppler shift in the frequency of the IF signal obtained from radar return from the sea surface as given by (29).
$\Delta f'$	Frequency shift given by (19) necessary to align the return spectral waveform properly with the half-power point of the leading edge of the waveform in the tracking gate. This frequency shift is related by (5) to the error Δt_d in the time lag between transmitted and deramping chirps.
$\Delta f'_{\max}$	Maximum frequency shift of the return waveform that can be achieved by applying a phase rotation in the time domain to the IF signal, as given by (26).
$\Delta f'_{\min}$	Resolution of the frequency shift of the return waveform that can be achieved by applying a phase rotation in the time domain to the IF signal, as given by (24).
FFT	Fast Fourier transform.
g	Decay factor for a Gaussian antenna pattern used in (52) to express the antenna gain in terms of frequency in the IF signal.
G	Antenna gain along the antenna boresight (appendix A).
$G(f)$	Antenna gain pattern expressed in terms of frequency. For an antenna gain that is a Gaussian function of the angle θ_L relative to the antenna boresight (Fig. 10), $G(f)$ is related to $G(\theta_L)$ by (52).
$G(\theta_L)$	Antenna gain pattern expressed in terms of angle θ_L relative to the antenna boresight (Fig. 10).
γ	Pointing angle of the antenna boresight relative to vertical (Fig. 1).
h	Sea surface height relative to mean sea level.
h_{med}	The median sea surface height as defined by (28).
H	Radius of the satellite orbit, equal to the

	radius of the earth R_e plus the satellite altitude R_0 (appendix A).
$H(f-f_0)$	Heaviside step function, equal to 0 for $f<f_0$ and 1 for $f\geqslant f_0$.
$H_{1/3}$	Significant wave height, equal to four times the standard deviation σ of sea surface height. This corresponds approximately to the crest-to-trough height of the ⅓ largest waves in the altimeter footprint.
Δh_D	Range error due to the two-way Doppler shift in the frequency of the IF signal given by (31).
IF	Acronym used to indicate the intermediate frequency signal obtained by differencing the signal returned from the sea surface with a deramping chirp generated internally by the altimeter.
j	Index corresponding to gate number in the return waveform.
k	Half of the total number of neighboring waveform gates used to form the middle gate according to (18).
L	Distance along the sea surface measured from satellite nadir along a flat earth (Figs. 10 and 19).
L'	Arc length along the sea surface measured from satellite nadir along a spherical-earth surface (Fig. 19).
m	Index corresponding to the tracking gate (equal to gate 30.5 for SEASAT and GEOSAT, and midway between gates 32 and 33 for TOPEX) in the return waveform.
n	Index corresponding to sequential $1/20$ s update cycle used by the ATU to form average waveforms and adjust the tracking of the half-power point on the leading edge of the waveform.
N	Number of samples of the IF signal processed by the ATU.
N_{agc}	Number of range gates centered on the tracking gate that are included in the AGC gate given by (17).
N_G	Scaling factor in the AGC gate (17) to account for plateau droop in the return waveform due to the antenna gain pattern.
$p(h)$	Probability density function for the sea surface height h (section 5d).
$P(t)$	Time series of power returned from the sea surface in pulse-limited altimetry (section 2, Fig. 4).
$P(f)$	Power spectrum as a function of frequency of the IF signal obtained from the radar return from a small region on the sea surface with continuous sea surface height probability distribution (Fig. 9b).
$P_3(f)$	Power spectrum of the IF signal for the idealized case of only three reflecting points on the sea surface (Fig. 9a).
$P_{\max}$	Maximum of the power time series $P(t)$ returned from the sea surface in pulse-limited altimetry (section 2, Fig. 4).
P_{noise}	Background noise in the power time series $P(t)$ returned from the sea surface in pulse-limited altimetry (section 2, Fig. 4).
P_r	Total power of returned signal in the radar equation (41) and (43).
P_T	Total power of transmitted signal in the radar equation (41) and (43).
$\phi(t)$	Phase shift applied in the time domain to the IF signal to introduce an effective time delay in the deramping chirp and align the return waveform properly relative to the tracking gate (section 4).
$\phi_{\max}$	Maximum phase adjustment that can be applied in the time domain to the IF signal to align the return waveform properly relative to the tracking gate (section 4).
$\phi_{\min}$	Resolution of the phase adjustment that can be applied in the time domain to the IF signal to align the return waveform properly relative to the tracking gate (section 4).
$\psi(t)$	Time series of the IF signal (section 4).
$\Psi(f)$	Fourier transform of the IF signal time series (section 4).
Q	Sweep rate of the transmitted chirp. For a chirp sweep period τ and a total frequency range ΔF, the sweep rate is $Q=\Delta F/\tau$.
R_0	Altitude of the satellite (the range from the altimeter antenna to nadir mean sea level) (Fig. 10).
R_e	Radius of the earth (approximately 6371 km).
R_L	Range from the altimeter antenna along off-nadir angle θ_L to a point on the sea surface a distance L from nadir on a flat earth (appendix A, Fig. 19). In section 3, R_L refers to the slant range to a spherical earth, denoted by R'_L in section A3; the prime is dropped for convenience in section 3.
R'_L	Range from the altimeter antenna along off-nadir angle θ_L to a point on the sea surface a distance L' from nadir on a spherical earth (appendix A, Fig. 19).
Δr_L	The range difference between the slant range to the sea surface on a flat earth and the satellite altitude R_0 (appendix A, Fig. 19). In section 3, Δr_L is the range difference between R_0 and the slant range to a spherical earth equal to $\Delta r'_L$

	in section A3; the prime is dropped for convenience in section 3 (Figs. 10 and 19).
$\Delta r'_L$	The range difference between R'_L and R_0 on a spherical earth (appendix A, Fig. 19) referred to as Δr_L in section 3.
s	One-half of the sum of the three sides of the triangle (35) formed by the satellite location, the center of the earth, and the point where the off-nadir angle θ'_L intersects the spherical earth (appendix A, Fig. 19).
s'	One-half of the sum of the three sides of the triangle (46) formed by the satellite location, the center of the earth, and the point where the off-nadir angle θ_L intersects the spherical earth (appendix A, Fig. 19).
$S_1(f)$	The spectral power as a function of frequency of the IF signal as given by (12) for an ideal antenna with wide beamwidth and a uniform gain of 1 (Fig. 11a).
$S_G(f)$	The spectral power as a function of frequency of the IF signal as given by (13) for a realistic antenna with gain of G (Fig. 11b).
S_j	The spectral power in range gate j of the return spectral waveform.
S_{agc}	The "AGC gate" defined by (17), equal to the scaled sum of spectral values in N_{agc} range gates centered on the tracking gate.
$S_{\max}$	The maximum spectral power in a return waveform.
S_{mid}	The "middle gate" defined by (18), equal to the average of $2k + 1$ spectral values near tracking gate m at the half-power point of the leading edge of the return waveform.
σ	The radar scattering cross section of the sea surface in the radar equation (41) and (43) in appendix A. Also used in section 5 and Fig. 16 to denote the standard deviation of sea surface height.
σ_0	Flat-earth approximation of the normalized radar cross section, defined to be σ divided by the sea surface area A on a flat earth illuminated by the antenna (appendix A).
σ'_0	The normalized radar cross section for a spherical earth, defined to be σ divided by the sea surface area A' on a spherical earth illuminated by the antenna (section A2).
SWH	Significant wave height, equal to four times the sea surface height standard deviation.
T	Transmittance of the atmosphere (defined to range from 1 for a transparent atmosphere to 0 for an opaque atmosphere) in the radar equation (41) and (43) in appendix A.
t_0	The two-way travel time between the satellite and mean sea level at satellite nadir.
t_C	The time lag between transmitted chirp and the received chirp reflected from a wave crest in the idealized case of only three reflecting points on the sea surface (Figs. 7 and 8).
t_d	The time lag between the transmitted and deramping chirps. For proper tracking, t_d is equal to the two-way travel time t_0 between the satellite and mean sea level at satellite nadir. More generally, $t_d = t_0 - \Delta t_d$, where Δt_d is the error in the timing of the deramping chirp.
$t_d(n)$	The time lag between transmitted and deramping chirps for update cycle n in the recursion relations (21).
$\dot{t}_d(n)$	The change of the time lag between transmitted and deramping chirps from update cycle $(n - 1)$ to update cycle n in the recursion relations (21) (units of time).
$\ddot{t}_d(n)$	The rate of change in time lag between transmitted and deramping chirps from update cycle $(n - 1)$ to update cycle n (units of time). This term is not included in the recursion relations (21) for the α–β tracker.
t_L	The two-way travel time between the satellite and mean sea level a distance L from satellite nadir.
t_T	The time lag between transmitted chirp and the received chirp reflected from a wave trough in the idealized case of only three reflecting points on the sea surface (Figs. 7 and 8).
$t'_d(n)$	The corrected time lag between transmitted and deramping chirps given by (22a) that would apply to update cycle n if the return waveforms were noise free.
$\dot{t}'_d(n)$	The corrected timing change from update cycle $(n - 1)$ to update cycle n given by (22b) that would apply if the return waveforms were noise free (units of time).
δt	Sample interval in the time domain for the N discrete samples of the IF signal.
δt_{eff}	Effective two-way travel time resolution given by (15) for a spectral waveform sampled at frequency interval δf.
Δt	The two-way travel time difference measured relative to the time t_0 when the return signal from mean sea level at

	satellite nadir is received. This time difference is related to frequency in the IF signal by (7).
Δt_d	Error in the time lag t_d between the transmitted and deramping chirps given by (20) due to tracking misalignment of the return waveform. For a two-way travel time t_0 from nadir mean sea level, the tracking error is $\Delta t_d = t_0 - t_d$.
Δt_D	Two-way travel time delay (30) due to Doppler shift of the transmitted signal.
Δt_L	The difference given by (10) between the time t_L that the signal from mean sea level a distance L from satellite nadir is received and the time t_0 that the signal from nadir mean sea level is received.
$\Delta t'_L$	The difference given by (50) between the time that the signal from mean sea level along off-nadir angle θ_L is received from a spherical earth and the time that the signal from nadir mean sea level is received (section A3), referred to as Δt_L in section 3.
$\Delta t_d{}^{\max}$	The maximum effective adjustment of the time lag between transmitted and deramping chirps given by (27) that can be obtained by adding a phase shift in the time domain to the IF signal.
$\Delta t_d{}^{\min}$	The resolution of effective adjustments of the time lag between transmitted and deramping chirps given by (25) that can be obtained by adding a phase shift in the time domain to the IF signal.
τ	The sweep period of the altimeter transmitted chirp.
θ	The angle corresponding to the half-power point of the antenna gain pattern (Figs. 1b and 10).
θ_L	The angle relative to the antenna boresight of the vector from the altimeter antenna to a point on the sea surface a distance L from satellite nadir along a flat earth surface (Figs. 10 and 19).
θ'_L	The angle relative to the antenna boresight of the vector from the altimeter antenna to a point on the sea surface an arc length L' from satellite nadir along a spherical earth surface (section A1, Fig. 19).
v	The vertical component of the velocity of the satellite relative to the sea surface at nadir in the expression (29) for frequency Doppler shift.
ω	Angle measured from the center of the earth subtended by the arc length defined by the point at satellite nadir and the intersection of the off-nadir angle θ_L with the sea surface on a spherical earth (appendix A, Fig. 19).

REFERENCES

Barrick, D. E., and B. J. Lipa, 1981: SEASAT altimeter tracker bias studies and simulations. Tech. Memo., Nat. Oceanic Atmos. Admin., Environ. Res. Lab., Boulder, CO.

Born, G. H., M. A. Richards and G. W. Rosborough, 1982: An empirical determination of the effects of sea-state bias on the SEASAT altimeter. *J. Geophys. Res.*, **87**, 3221–3226.

Briscoe, M. G., 1986: A primer on the U.S. contribution to the World Ocean Circulation experiment. U.S. WOCE Planning Rep. 4, 35 pp., U.S. Planning Office for WOCE.

Brown, G. S., 1977: The average impulse response of a rough surface and its applications. *IEEE Trans. Antennas Propag.*, **AP-25**, 67–74.

Caputi, W. J., 1971: Stretch: a time transformation technique. *IEEE Trans. Aerospace and Electron. Sys.*, **AES-7**, 269–278.

Chelton, D. B., 1988: WOCE/NASA Altimeter Algorithm Workshop. U.S. WOCE Tech. Rep. 2, 70 pp., U.S. Planning Office for WOCE.

——, and P. J. McCabe, 1985: A review of satellite altimeter measurement of sea surface wind speed: with a proposed new algorithm. *J. Geophys. Res.*, **90**, 4707–4720.

——, and F. J. Wentz, 1986: Further development of an improved altimeter speed algorithm. *J. Geophys. Res.*, **91**, 14,250–14,260.

——, K. J. Hussey and M. E. Parke, 1981: Global satellite measurements of water vapour, wind speed and wave height. *Nature*, **294**, 529–532.

Cheney, R. E., L. L. Miller, B. C. Douglas and R. W. Agreen, 1987: Monitoring equatorial Pacific sea level with GEOSAT. *Johns Hopkins APL Tech. Dig.*, **8**, 245–250.

Douglas, B. C., and R. W. Agreen, 1983: The sea-state correction of GEOS-3 and SEASAT altimeter data. *J. Geophys. Res.*, **88**, 3254–3260.

Goldhirsch, J., 1983: Rain cell size statistics as a function of rain rate for attenuation modeling. *IEEE Trans. Antennas Propag.*, **AP-31**, 799–801.

Hancock, D. W., R. G. Forsythe and J. Lorell, 1980: SEASAT altimeter sensor file algorithms. *IEEE J. Oceanic Eng.*, **OE-5**, 93–99.

Hayne, G. S., 1980: Radar altimeter mean return waveform from near-normal incidence ocean surface scattering. *IEEE Trans. Antennas Propag.*, **AP-28**, 687–692.

——, 1981: Radar altimeter waveform modeled parameter recovery. NASA Tech. Memo. TM-73294, NASA Wallops Flight Center.

——, and D. W. Hancock, 1982: Sea-state related altitude errors in the SEASAT radar altimeter. *J. Geophys. Res.*, **87**, 3227–3231.

——, and ——, 1987: Waveform analysis for GEOSAT day 96. *Johns Hopkins APL Tech. Dig.*, **8**, 255–259.

Lipa, B. J., and D. E. Barrick, 1981: Ocean surface height-slope probability density function from SEASAT altimeter echo. *J. Geophys. Res.*, **86**, 10,921–10,930.

MacArthur, J. L., 1978: SEASAT-A radar altimeter design description. Johns Hopkins University, Appl. Phys. Lab., Rep. 5DO-5232.

——, and P. V. K. Brown, 1984: Altimeter for the Ocean Topography Experiment (TOPEX). Soc. Photo-Optical Instr. Engin., Vol. 481, *Recent Advances in Civil Space Remote Sensing*, 172–180.

——, P. C. Marth and J. G. Wall, 1987: The GEOSAT radar altimeter. *Johns Hopkins A.P.L. Tech. Digest*, **8**, 176–181.

Marks, F. D., 1985: Evolution of the structure of precipitation in Hurricane Allen (1980). *Mon. Wea. Rev.*, **113**, 909–930.

Maul, G. A., 1985: *Introduction to Satellite Oceanography.* Martinus Nijhoff Pub., 606 pp.

McGoogan, J. T., L. S. Miller, G. S. Brown and G. S. Hayne, 1974: The S-193 radar altimeter experiment. *Proc. IEEE*, **62**, 793–803.

Monaldo, F. M., J. Goldhirsch and E. J. Walsh, 1986: Altimeter height measurement error introduced by the presence of variable cloud and rain attenuation. *J. Geophys. Res.*, **91**, 2345–2350.

Nowlin, W. D., 1987: Status of U.S. planning for WOCE. *Bull. Amer. Meteor. Soc.*, **68**, 1559–1565.

Rodriguez, E., 1988: Altimetry for non-Gaussian oceans: height biases and estimation of parameters. *J. Geophys. Res.*, **93,** 14 107–14 120.

——, and B. Chapman, 1989: Extracting ocean surface information from altimeter returns: the deconvolution method. *J. Geophys. Res.*, (in press).

Skolnik, D. L., Ed., 1970: *Radar Handbook,* McGraw-Hill Book Co.

Srokosz, M. A., 1986: On the joint distribution of surface elevations and slopes for a nonlinear random sea, with an application for radar altimetry. *J. Geophys. Res.*, **91,** 995–1006.

Stanley, H. R., 1979: The GEOS-3 Project. *J. Geophys. Res.*, **84,** 3779–3783.

Stewart, R. H., 1985: *Methods of Satellite Oceanography,* University of California Press, Berkeley, Calif., 360 pp.

Tapley, B. D., G. H. Born and M. E. Parke, 1982: The SEASAT altimeter data and its accuracy assessment. *J. Geophys. Res.*, **87,** 3179–3188.

TOPEX Science Working Group, 1981: Satellite altimetric measurements of the ocean. Doc. 400-111, Jet Propul. Lab., Pasadena, Calif.

Townsend, W. F., 1980: An initial assessment of the performance achieved by the SEASAT altimeter. *IEEE J. Oceanic Eng.*, **OE5,** 80–92.

——, J. T. McGoogan and E. J. Walsh, 1981: Satellite radar altimeters—present and future oceanographic capabilities. *Oceanography from Space,* J. F. R. Gower, Ed., Plenum Press, 625–636.

Ulaby, F. T., T. F. Haddock and R. T. Austin, 1988: Fluctuation statistics of millimeter-wave scattering from distributed targets. *IEEE Trans. Geosci. Remote Sens.*, **26,** 268–281.

Vakman, D. E., 1968: *Sophisticated Signals and the Uncertainty Principal in Radar.* Springer–Verlag.

Walsh, E. J., 1979: Extraction of ocean wave height and dominant wavelength from GEOS-3 altimeter data. *J. Geophys. Res.*, **84,** 4003–4010.

——, 1982: Pulse-to-pulse correlation in satellite radar altimeters. *Radio Sci.*, **17,** 786–800.

——, F. M. Monaldo and J. Goldhirsch, 1984: Rain and cloud effects on a satellite dual-frequency radar altimeter system operating at 13.5 and 35 GHz. *IEEE Trans. Geosci. and Remote Sens.*, **GE-22,** 615–622.

——, F. C. Jackson, E. A. Uliana and R. N. Swift, 1989: Observations on electromagnetic bias in radar altimeter sea surface measurements. *J. Geophys. Res.*, (accepted).